Raman Spectroscopy of Metallic Carbon Nanotubes

by

Hootan Farhat

B.A.Sc., University of Toronto (2004)

Submitted to the Department of Materials Science and Engineering
in partial fulfillment of the requirements for the degree of

Doctor of Philosophy

at the

MASSACHUSETTS INSTITUTE OF TECHNOLOGY

June 2010

Author .....
Department of Materials Science and Engineering
May 21, 2010

Certified by .....
Jing Kong
Associate Professor
Thesis Supervisor

Accepted by .....
Christine Ortiz
Chairman, Department Committee on Graduate Theses

Raman Spectroscopy of Metallic Carbon Nanotubes

by

Hootan Farhat

Submitted to the Department of Materials Science and Engineering
on May 21, 2010, in partial fulfillment of the
requirements for the degree of
Doctor of Philosophy

Abstract

Metallic carbon nanotubes are one dimensional conductors that are both technologically promising for electronic applications, and scientifically interesting for studying the physics of low dimensional materials. In this thesis, we present a detailed study of the inelastic light scattering (Raman) spectrum of individual metallic carbon nanotubes, with a focus on the influence of electronic excitations and charged carriers. We have demonstrated that the frequency and linewidth of certain phonon modes of metallic carbon nanotubes depend strongly the Fermi energy, because they couple strongly to low lying electron hole pairs. Next, we report the first experimental observation of *electronic* Raman scattering in carbon nanotubes. This observation demonstrates that the same electron-hole pairs that participate in damping the optical phonons of metallic carbon nanotubes, may themselves scatter light, thus giving rise to an electronic Raman spectrum. An analysis of the Fermi level and laser energy dependence of the electronic Raman and phonon Raman contributions allows us to explain the asymmetric lineshape of the G-band phonon modes in terms of a Fano interference. In another experiment, we have shown that the charge-induced expansion and contraction of the the graphitic C-C bond length is different for metallic and semiconducting nanotubes. Finally, we have measured the Stokes and antiStokes intensities of the Raman modes in electrically contacted metallic nanotubes in order to determine their phonon populations during high-field electrical transport. The experiments reported here, have helped to clarify the origin of several features in the Raman spectra of metallic carbon nanotubes that have been heavily debated in recent years. These result also shed light on the way electronic excitations and charged carriers affect the physical properties of metallic carbon nanotubes.

Thesis Supervisor: Jing Kong
Title: Associate Professor

Acknowledgments

The thesis would not have been possible without the help of many people. I would like to thank my adviser Jing Kong for being an excellent scientific mentor. Most people will agree that Jing is the kindest and most approachable professor that they have ever met. I have greatly benefited from her patience, knowledge and willingness to help in any situation. I have also had the opportunity to work under the guidance of Prof. Mildred S. Dresselhaus. Millie has taught me the importance of understanding the 'big picture' without overlooking the smallest detail. I would like to thank Prof. Francesco Stellacci and and Prof. Nicola Marzari for their helpful feedback as members of my thesis committee. I would also like to thank Dr. Gene Dresselhaus who over the years has entertained me with his dark humor, political commentary, and historical anecdotes.

I have had the opportunity to take part in some very fruitful collaborations. I would like to thank Prof. Riichiro Saito and and Dr. Ken-ichi Sasaki for their theoretical guidance without which I would not have been able to understand my experimental results. I am also grateful to Stephane Berciaud and Prof. Tony Heinz for introducting me to Rayleigh scattering spectroscopy and colloborating closely with me on the electronic Raman scattering project. Martin Kalbac has worked closely with me on many projects and I thank him for all that he has taught me about electrochemistry.

My thesis work would not have been possible without the help of other students in our lab. I extend my gratitude to: Hyungbin Son, for building much of our lab out of scratch and for teaching me intricacies of his Raman system; Alfonso Reina Cecco and Mario Hofmann for the grueling hours spent developing nanotube growth recipes that I later used in my project; and Dan Nezich for 'helpful discussions' about physics and device fabrication. Finally, thanks to all the members of the the NME and MGM groups that have contributed to the cooperative and friendly atmosphere of our lab.

Contents

List of Figures

Chapter 1

Introduction

A carbon nanotube is cylinder of sp^2 carbon whose radial dimension is on the order of a nanometer. Within a diameter range of $1nm < d_t < 2nm$, there are 151 unique ways that a seamless cylinder can be constructed, each of which gives rise to a unique electronic structure. The diversity of physical behaviors arising from the subtlest differences in structure is what makes carbon nanotubes so interesting and challenging to scientists and what has, so far, plagued their technological adoption. While each nanotube species is unique, their electronic properties fall into two categories, metals and semiconductors. Metallic nanotubes are similar to semiconducting nanotubes with the addition of mobile carriers and low energy excitations.

To physicists, metallic carbon nanotubes are interesting because they are one of very few accessible 1D metals. Since a nanotube is constructed from a rigid graphene backbone, it is not susceptible to Peierls instabilities, as a true 1D metal should be. Nonetheless, electrons in SWNTs occupy a single one dimensional electronic band even, at room temperature. Recent observations of interest in the metallic carbon nanotube literature include a Mott insulating state, an exciton in a metal, and strong Kohn anomalies in the phonon dispersion. From a technological perspective, metallic carbon nanotubes are sought out for their low resistance and high current carrying capacity for both electronic interconnect and conductive composite applications. For these potential applications an understanding of the scattering mechanism for current carrying carriers is paramount.

Raman spectroscopy has emerged as the most useful tool for characterizing carbon nanotubes, mostly because it can reveal the detailed structure of the carbon nanotube. However, Raman spectroscopy provides far more information that simply the structure. For instance, this spectroscopic technique can be used to gain information about nanotube metallicity, strain, doping and temperature with a simple optical measurement. In this thesis, we use Raman spectroscopy as a primary tool and combine it with methods developed for studying electron transport and electrochemistry to learn about how electrons interact with vibrations (through the electron-phonon interaction) and with other electrons (through the Coulomb interaction) as well as with the lattice.

This thesis is organized as follows: Chapter 2 provides an introduction to the physical structure and the electronic and vibrational properties of carbon nanotubes. In chapter 3, we discuss Fermi level-dependent Raman measurements that shed light on the way that electronic excitation interact with vibrational modes of metallic SWNTs. Next, in chapter 4, we provide evidence of these same electronic excitations scattering light and giving rise to an electronic Raman spectrum. Chapter 5 addresses the differences between metallic and semiconducting nanotubes in the context of charge-induced lattice deformation. Chapter 6 is a study of how energy is transfered to phonons when large currents are passed through a SWNT. We conclude a summary and suggested future work in Chapter 7.

Chapter 2

Background

This chapter introduces elements of the physical properties of carbon nanotubes that are necessary in order to follow the experimental results presented in the thesis.

2.1 Structure and notation

A carbon nanotube is a seamless cylinder of graphene, a two dimensional hexagonal lattice of sp^2 bonded carbon. There are a number a ways that a graphene sheet could be rolled up to yield a closed structure. These structures can be described by the wrapping vector,

$$\mathbf{C}_h = n\mathbf{a_1} + m\mathbf{a_2}, \tag{2.1}$$

which is depicted in Fig. 2-1. Here, $(\mathbf{a_1}, \mathbf{a_2})$ are the unit vectors of the graphene lattice and (n, m) are integer indices that uniquely define the structure of a SWNT [1]. The structure may also be described in terms of its diameter d_t and chiral angle θ given by,

$$d_t = C_h/\pi = \sqrt{3}a_{CC}(m^2 + mn + n^2)^{1/2}/\pi \tag{2.2}$$

$$\theta = tan^{-1}[\sqrt{3}m/(m + 2n)]). \tag{2.3}$$

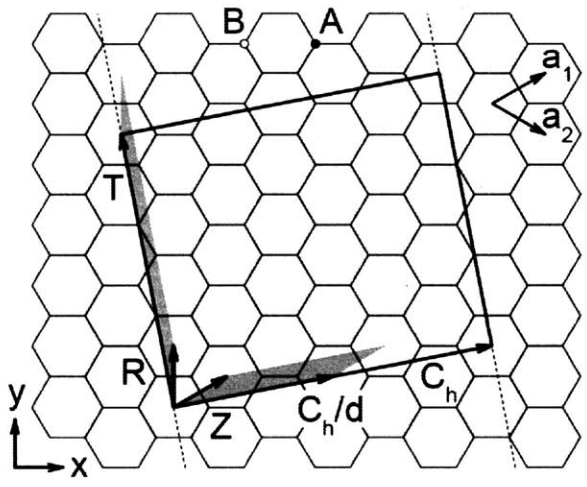

Figure 2-1: An illustration of the wrapping vector, C_h, used to describe the structure of a SWNT in terms its basis vectors a_1 and a_2 [2].

Carbon nanotubes with (n, m) indices of the form $(N, 0)$ have $\theta = 30°$ and are referred to as zigzag nanotubes, while those of the form (N, N) have $\theta = 30°$ and are referred to as armchair nanotubes. Zigzag and armchair nanotubes are achiral nanotubes, while SWNTs with chiral angles $0 \leq \theta \leq 30°$, are referred to as chiral nanotubes.

2.2 Electronic structure

Many of the electronic properties of SWNTs stem from those of graphene. Graphene has a hexagonal Brillouin zone with two inequivalent vertices called the K and K' points. The zone center is called the Γ point and the midpoint of K and K' is the M point (see Fig. 2-2). A simple tight binding calculation [1] of the electronic structure of graphene yields the following:

$$\omega(\mathbf{k}) = \pm\gamma_o\sqrt{(1 + 4\cos(\frac{\sqrt{3}k_x a}{2})\cos(\frac{k_y a}{2}) + 4\cos^2(\frac{k_y a}{2}))} \tag{2.4}$$

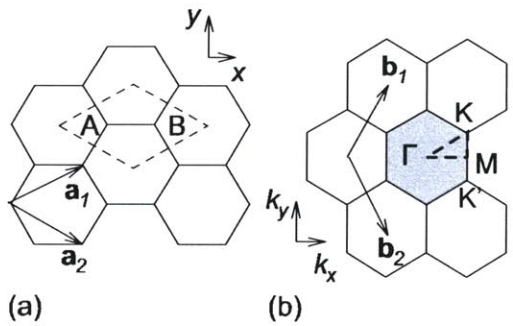

Figure 2-2: The real space of reciprocal space lattice of graphene, illustrating the important symmetry points [2].

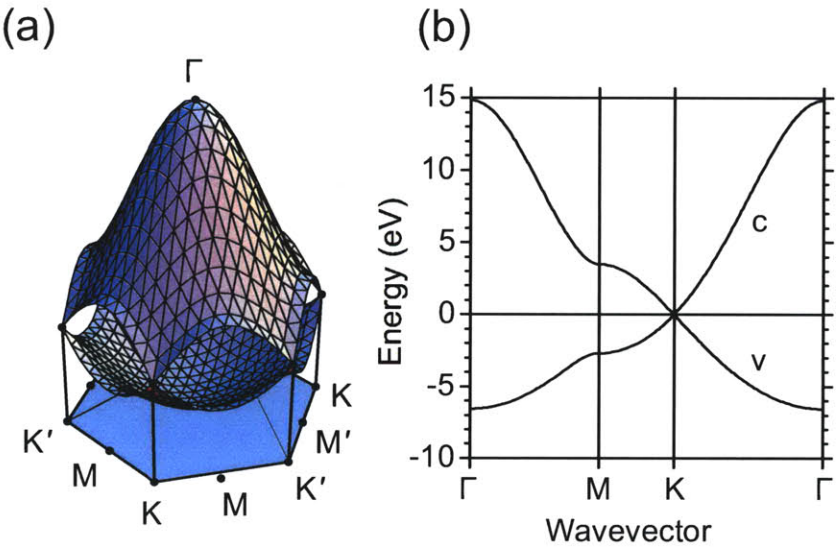

Figure 2-3: The electronic band structure of graphene $E(k)$ within the 1st Brillouin Zone

which captures the important features of the electronic dispersion, namely that the conduction and valence bands touch each other at the vertices of the hexagonal Brillouin zone, as shown in Fig. 2-3. Around these points, the dispersion relation for the electronic bands are linear in wavevector k, resulting in two cones.

To first order, the electronic structure of SWNT can be obtained by imposing periodic boundary conditions on the electronic wavefunctions along the circumference of the nanotube. This results in a discretization of states in the circumferential direction, and reduces the phase space to a series of lines, as show in in Fig. 2-5 a), whose spacing is inversely proportional to the SWNT diameter d_t and whose

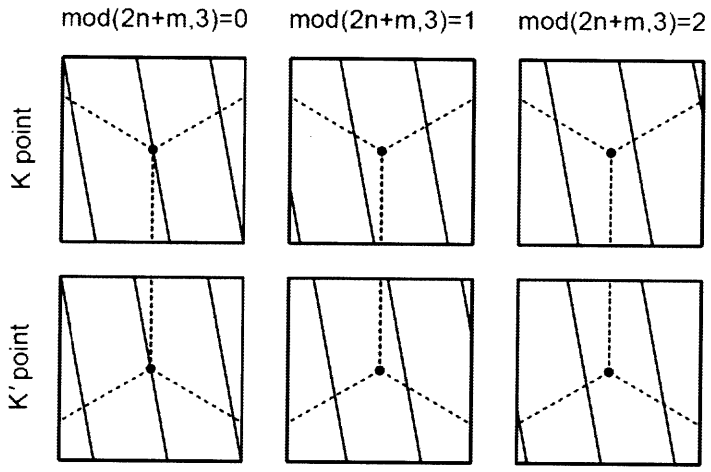

Figure 2-4: An illustration of how the cutting lines of different mod($2n+m$,3) families intersect near the K-point [2]. When a cutting line intersects the K or K' point, a metallic nanotube results.

orientation with respect to the Brillouin zone depends on the chiral angle θ. The resulting one-dimensional electronic band structure of SWNT is then comprised of a series of conical cross sections. These cuts in phase space are referred to as 'cutting lines' [1]. When a cutting line intersects with the K or K' point, the resulting 1D subbands are linear bands that intersect at the Fermi level. Those cutting lines which intersect the Dirac cones away from the corners of the Brillouin zone result in hyperbolic subbands whose conduction and valence band are separated by a gap. It can be shown, that nanotubes which satisfy the conditions mod($2n + m$,3)=0, have a cutting line that intersects the K-point. These SWNTs are referred to as metallic nanotubes because their linear band structure does does not have a bandgap at the Fermi level. Those tubes satisfying mod($2n + m$,3)=$\pm$1 have hyperbolic bands and bandgaps and are referred to as semiconducting nanotubes. The intersections of the cutting lines near the K-point for the 3 types of nanotubes are illustrated in Fig. 2-4. In Fig. 2-5, we show the cutting lines and calculated band structure for an armchair metallic tube Fig. 2-5 a), for a zigzag metallic tube Fig. 2-5 b) and for a zigzag semiconducting tube 2-5 c).

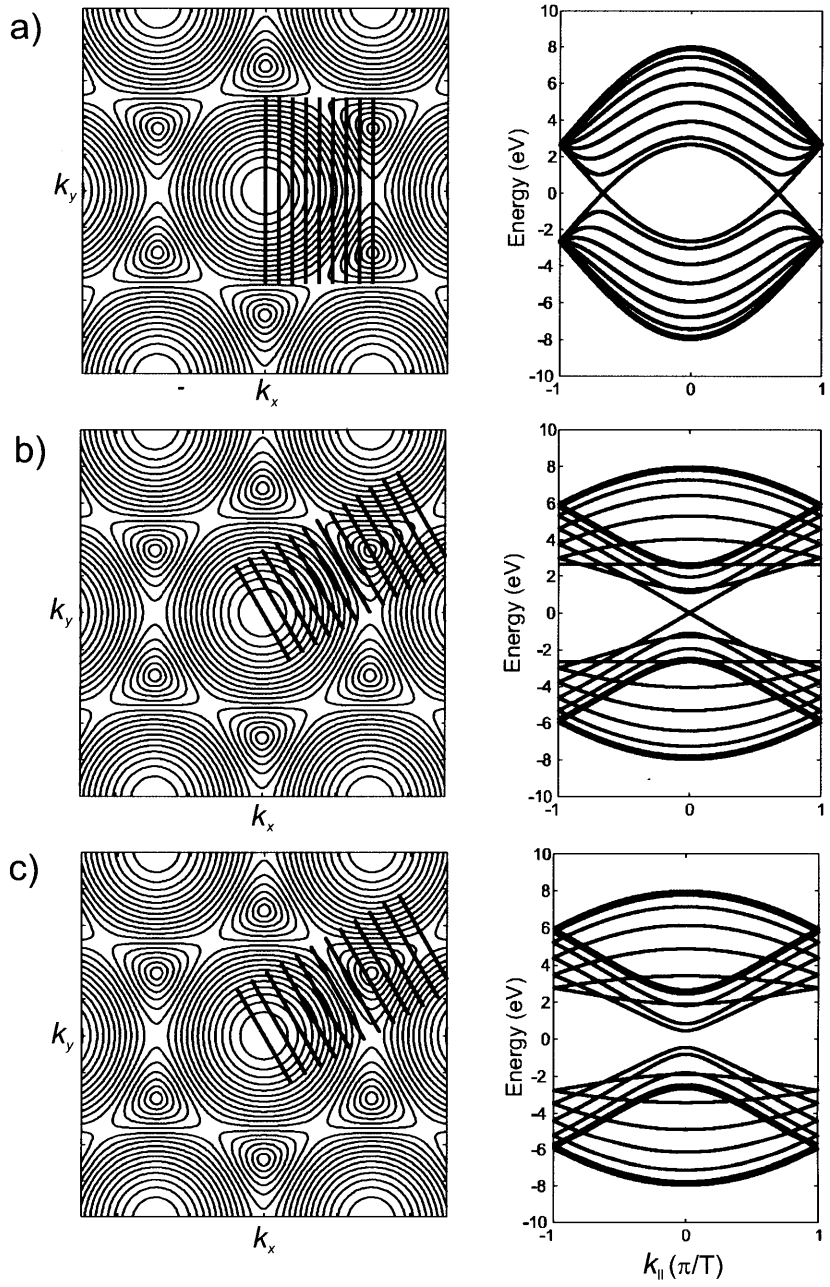

Figure 2-5: Cutting lines superposed on contour plots of the electronic structure of graphene and the resulting 1D subbands for several SWNTs. a) an (8,8) armchair metallic nanotube b) a (12,0) zigzag metallic nanotube c) and an (11,0) semiconducting nanotube.

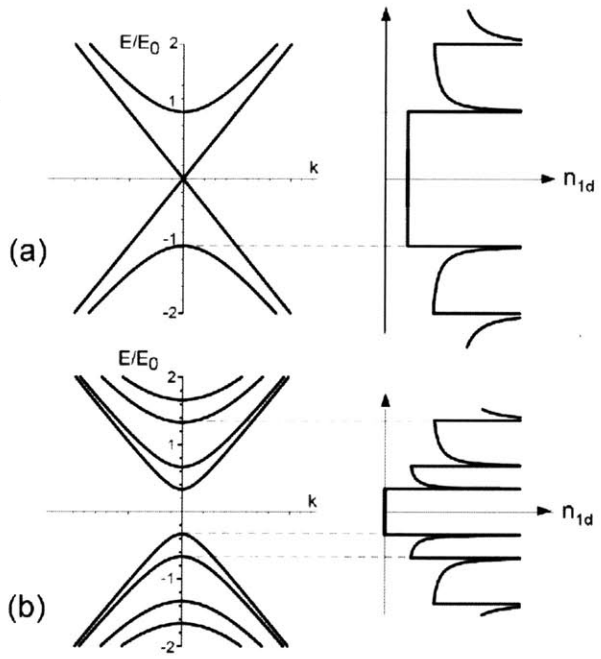

Figure 2-6: The electronic structure (left) and corresponding density of states (right) for a) a metallic nanotube, and b) a semiconducting nanotube.

2.2.1 Density of states

In one dimension, the density of states (DOS) at the vertex of a parabolic band is singular and falls off as $1/\sqrt{E}$. The resulting asymmetric spike in the DOS is referred to as a van Hove singularity (VHS). The DOS for a linearly dispersive band is a constant. Figure 2-6 illustrates the DOS of semiconducting and metallic nanotubes. The DOS of semiconducting nanotubes, contains a series of VHSs corresponding to the band edges of each hyperbolic band. In the case of metallic nanotubes, there is a constant DOS at low energies that is followed by VHSs for each of its non linear bands [1].

2.2.2 Optical transitions

The large density of states at the edge of each hyperbolic band result in resonant optical transitions between these states. In a semiconducting nanotube, a transition energy from the i^{th} valence band to the j^{th} conduction band is referred to as E_{ij}. Dipole selection rules dictate that, for light polarized along the axis of the nanotube, only transitions between the corresponding VHSs in the conduction and valence bands ($i = j$) are permitted [1]. Therefore, a semiconducting nanotube has a series of strong optical absorptions peaks corresponding to transition across corresponding VHSs. These transitions are referred to as S_{ii} or E_{ii}^{S}. In metallic nanotubes, optical absorption across the linear bands is dipole forbidden by symmetry; however, the higher hyperbolic bands behave similarly to those of semiconductors regarding optical transitions. These transitions are interchangeably referred to as M_{ii} or E_{ii}^{M}.

When many-body interactions are taken into account, the optical transitions of S-SWNTs are found to excitonic with binding energies of $\sim 0.5eV$. For M-SWNTs the M_{ii} transition are also excitonic with binding energies of $\sim 50meV$ [3, 4] . Most of the physics presented in this thesis, however, can be understood within the simpler band-to-band transition picture described above.

2.2.3 Trigonal warping

When the electronic bands of graphene are assumed to be conical, the two equidistant cutting lines on either side of the K-point give rise to degenerate subbands that contribute to the first van Hove singularity in the DOS. Away from the Dirac point, the band structure deviates from its conical shape, becoming gradually more triangular. This results in a splitting of the M_{ii} VHS because the two equidistant subbands can now have different minima. This effect, called trigonal warping, is illustrated in Fig. 2-7. Here we see that the angle between the cutting lines and the symmetry axis of the K-point, affect the amount of splitting [5]. The splitting between the upper and lower parts of the VHSs, denoted M_{ii}^{+} and M_{ii}^{-}, is greatest for zigzag metallic nanotubes and is absent for armchair metallic nanotubes.

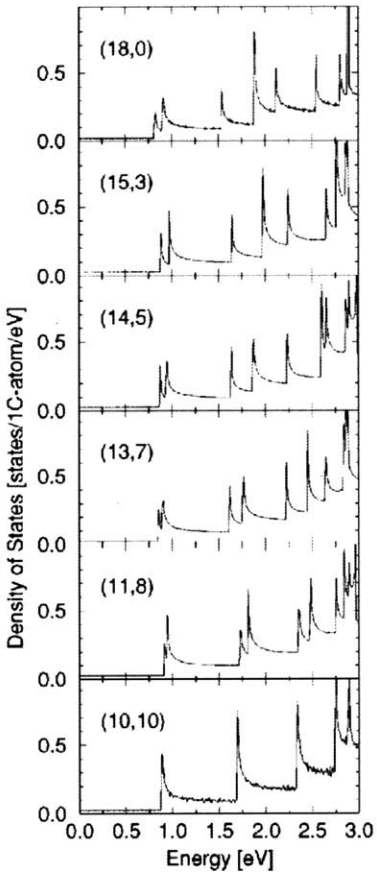

Figure 2-7: The DOS of several metallic nanotubes of different chiral angle showing the splitting of the VHSs due to trigonal warping. The effect is strongest for the zigzag tube (18,0) and is absent of the armchair tube (10,10) [5].

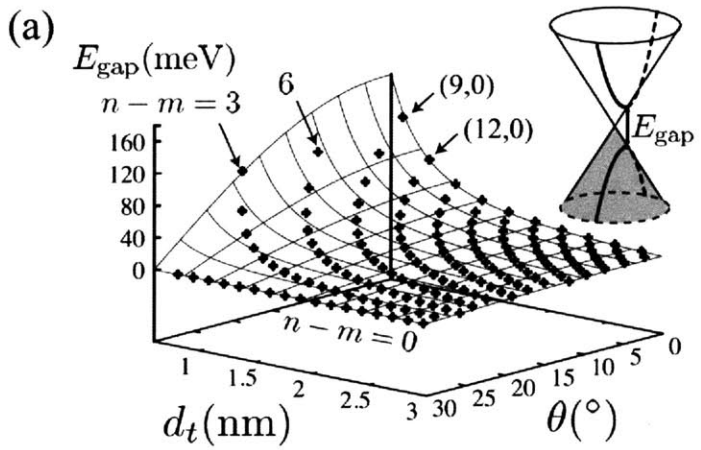

Figure 2-8: The magnitude of the curvature-induced minigap in metallic nanotubes as a function of the diameter and chiral angle [6]. The gap is largest for small diameter zigzag nanotubes.

2.2.4 Curvature-induced mini-gap in metallic nanotubes

In the zone folding scheme, all nanotubes satisfying mod($2n+m$,3)=0 are completely metallic; that is, their conduction and valence bands touch each other at the Fermi energy. When the curvature of the M-SWNT is taken into account, the strain in the radial direction causes the K-point to shift away from the cutting line, giving rise to a small gap [6]. The magnitude of the gap E_{gap} depends on the chiral angle and is given by:

$$E_{gap} = \frac{c}{d_t^2} cos(3\theta) \tag{2.5}$$

This gap is greatest in zigzag nanotubes because the radial strain causes the K-point to move perpendicular to the cutting lines. Conversely, E_{gap} is absent for armchair nanotubes because the K points move along the cutting line. Fig. 2-8 illustrates the magnitude of the gap as a function of the diameter and chiral angle.

2.3 Phonon structure and Raman spectroscopy

The phonon structure of graphene, plotted in Fig. 2-9 a), contains 3 optical and 3 acoustic branches. Again, by restricting the reciprocal lattice space to the cutting

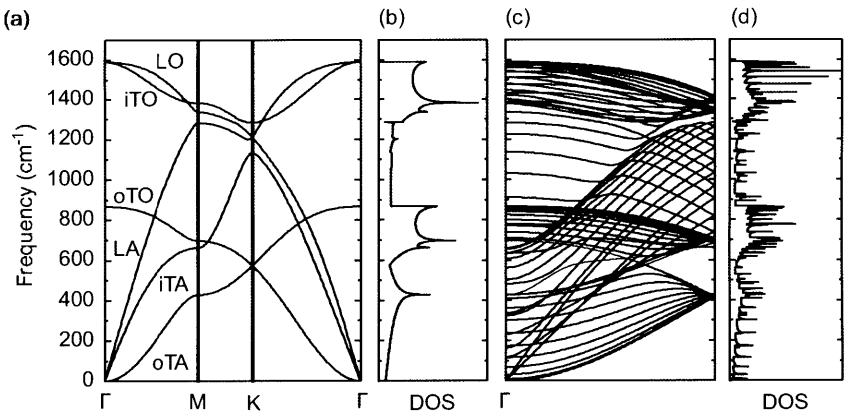

Figure 2-9: Phonon dispersion and phonon density of states and for graphene a) and b) and a SWNT c) and d) [2]

lines that are defined by the nanotube wrapping vector, a good approximation of the phonon dispersion of SWNTs can be obtained. Fig. 2-9 c) show the resulting $6N$ phonon branches for a SWNT with N cutting lines.

2.3.1 First-order Raman modes: The G-band and the Radial Breathing Mode

Raman scattering is the inelastic scattering of light by elementary excitation of a material. Raman scattered photons will have either lost or gained energy to an excitation. These two scattering processes are referred Stokes and antiStokes Raman scattering, respectively. Some elementary excitations that may Raman scatter light include phonons, individual and collective electronic excitations and magnons. Here we will describe some of the features of the Raman spectrum of carbon nanotubes associated with phonon excitations. A first-order Raman process involves scattering by a single phonon. Only phonons from the Γ point ($q = 0$) can participate in such a process because a photon can not compensate for any change in momentum. Two Γ-point Raman modes that are relevant to this thesis are the G-band and radial breathing mode.

(a) The G-band

The G-band, situated around $\sim 1600\text{cm}^{-1}$, corresponds to C-C stretching modes at the Γ point [2]. In graphene the G-band is a single peak composed of the degenerate longitudinal optical (LO) and an in-plane transverse optical (iTO) modes. The degeneracy at the Γ point of the two LO and iTO modes is lifted due to curvature and confinement effects leading to modes that are associated with bonds in the axial and radial directions. From zone folding of the LO and iTO modes we obtained each of these branches leads to N branches for a SWNT. However only three of these, namely those with A, E_1 and E_2 symmetries are Raman active [2]. For incident and scattered light that is polarized along the axis of the SWNT, only modes with A symmetry contribute to the intensity. Therefore, in practice, we can treat the G-band as having only two components. Namely, the LO and the TO modes are the modes which contribute the dominant intensity to the Raman spectra. Experimentally, two peaks, referred to as G^+ and G^-, are observed in the G-band, as illustrated in Fig. 2-10. For semiconducting nanotubes, the G^+ and G^- are assigned to the LO, and TO modes, while in metallic nanotubes the assignment is the opposite [7]. The details giving rise to this discrepancy are discussed in Chapter 3.

(b) The Radial Breathing Mode

The radial breathing mode (RBM) corresponds to the in-phase motion of all of the atoms in the radial direction. The corresponding mode in graphene is the out-of-plane bending mode, which is an acoustic phonon. However, the radial breathing mode of nanotubes is an optical phonon with frequencies in the range of $100-300\ \text{cm}^{-1}$ at the Γ point and can thus give rise to a first-order Raman feature. The RBM is an important mode, because of its inverse relationship to the nanotube diameter. Due to substrate and solvent interactions, an additional constant is required to experimentally match the RBM frequencies with the SWNT diameter [2]. The relation takes the form:

$$\omega_{\text{RBM}} = \frac{c_1}{d} + c_2 \tag{2.6}$$

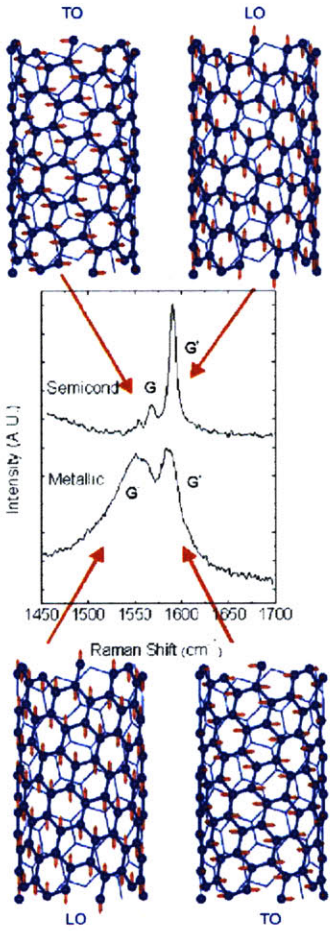

Figure 2-10: The G^+ and G^- components of the G-band and their corresponding phonon modes for semiconducting and metallic nanotubes [7].

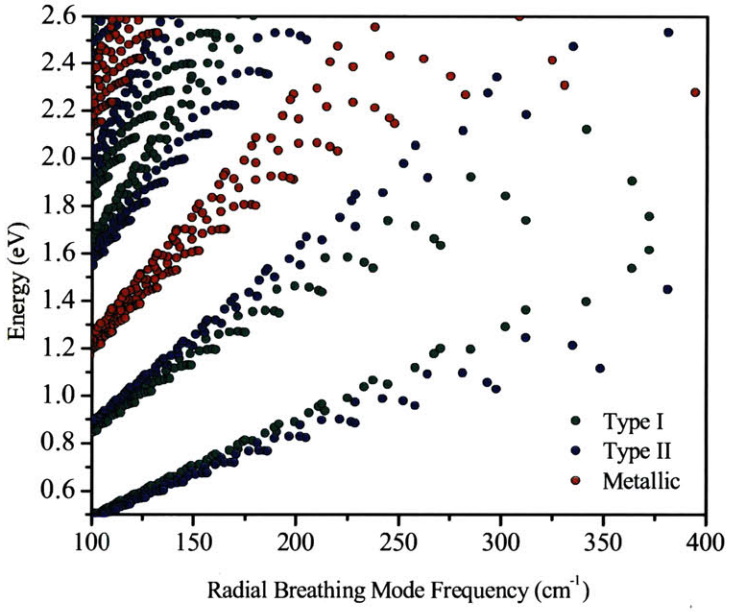

Figure 2-11: Kataura plot. Optical transition energies as a function of the RBM frequency. Red, blue and green markers correspond to metallic, mod($2n + m$,3)=1 and mod($2n + m$,3)=-1 nanotubes, respectively

where the constant c_1 depends on the elastic constants of sp^2 carbons and c_2 depends on environmental effects [8].

The Raman signal of nanotubes is strongly enhanced when the excitation energy corresponds to one of the optical transition energies. By finding the resonant energies of a nanotube using a tunable laser source, combined with the diameter information obtained from the RBM frequency, the (n, m) indices of the SWNT can be obtained [2]. Figure 2-11 is a Kataura plot, which maps out every (n, m) nanotube in terms of its optical transition energies and its corresponding RBM frequencies. Since the (n, m) of each data point is known, by mapping an experimentally measured SWNT ω_{RBM} onto this plot, the transition energy E_{ii} and electronic structure can be estimated.

2.3.2 Second-order Raman modes: the D and G' bands

Second-order Raman modes are those that originate from a phonon with a finite momentum ($q \neq 0$). The most studied double resonant features are the D and G' bands, which both involve the iTO phonon near the K-point. In order to conserve momentum a second scattering event is required. This momentum can be compensated through scattering by a defect, which is the case for the defect-activated D band feature. Momentum can also be compensated for the same phonon with and equal and opposite momentum, as in the case of the G' band [9]. For a particular SWNT, the phonon wavevector that satisfies these conditions depends strongly on the electronic structure and excitation energy that is used. Since the dispersion of the iTO peak near the K-point has a slope (Fig. 2-9), the frequencies of the D band and G' band features also depends on the electronic structure [9] of the SWNT.

Chapter 3

Phonon Softening in Metallic Carbon Nanotubes

In this chapter we investigate the coupling between phonons and electronic excitations in metallic carbon nanotubes. We begin by addressing the G-band Raman peak which, for years, has been known to exhibit a broad linewidth, a downshifted frequency, and an asymmetric lineshape in comparison to the G-band of S-SWNTs. By changing the occupancy of the linear electronic bands, we are able to block some of the electronic transitions that couple to the G-band, thereby suppressing the frequency renormalization and lifetime broadening brought about by this coupling. We then extend the study to the radial breathing mode phonon and show that it too experiences an, albeit weaker, energy renormalization but, in contrast, no lifetime broadening.

3.1 The G-band of metallic carbon nanotubes

As discussed in chapter 2, the G-band can typically be fit to a higher and a lower energy component denoted as the G^+ and G^- peaks [1]. The strongest contributions to the G-band are the A symmetry LO, and TO phonon modes whose atomic displacements are approximately oriented in the axial and radial directions [1], respectively, as illustrated in Fig. 3-1 c). Due to the curvature-induced softening of the radially

oriented bonds, the TO mode is expected to have a lower phonon energy than the LO mode. For this reason, the G^+ and G^- features of S-SWNTs are associated with the LO and TO modes, respectively [1]. While the same radial bond softening is expected for M-SWNTs, the LO/TO assignment is opposite to that of S-SWNTs for reasons that will be discussed below [7].

Figures 3-1 a) and b) show the G-band spectra of an S-SWNT and an M-SWNT. Both peaks in the spectrum of the S-SWNT have a linewidth of approximately 10 cm^{-1} and the G^+ peak exhibits a much larger intensity. The lineshape of the metallic G-band is strikingly different from that of the S-SWNT. The G^- peak for the M-SWNT is very broad, its frequency is significantly downshifted and it is skewed toward lower wavenumbers. Several works [10, 11, 12] have found that this peak fits better to a Breit-Wigner-Fano (BWF) lineshape,

$$I^{BWF}(\omega) = I_o \frac{[(q \cdot \Gamma + (\omega - \omega_o))]^2}{(\omega - \omega_o)^2 + \Gamma^2}, \tag{3.1}$$

than a Lorentzian profile. Further, in contrast to the spectrum of S-SWNTs, most of the integrated area of the metallic G-band is contained in the G^- peak, with the G^+ often being lost in the tail of the G^- feature.

Until recently there have been a number of conflicting experimental results pertaining the lineshape of the metallic G^- peak . The degree of broadening and asymmetry that has been reported is inconsistent across various works. Oron-Carl et al. [13] report that the G-band can be simply fit to two Lorentzian peaks, without using a BWF lineshape. Others [11] find that the broad asymmetric G^- feature is enhanced only in bundles, that it increases with bundle size and that it vanishes in the limit of an individual metallic nanotube. However, in 2007 Wu et al. [12] show that bundling is not a requirement for observing the broad G^- feature. By studying of the G-band of truly isolated metallic nanotubes whose (n, m) indices were assigned using Rayleigh scattering spectroscopy, Wu et al. reported that the broadening and asymmetry of the G-band are intrinsic features of isolated M-SWNTs .

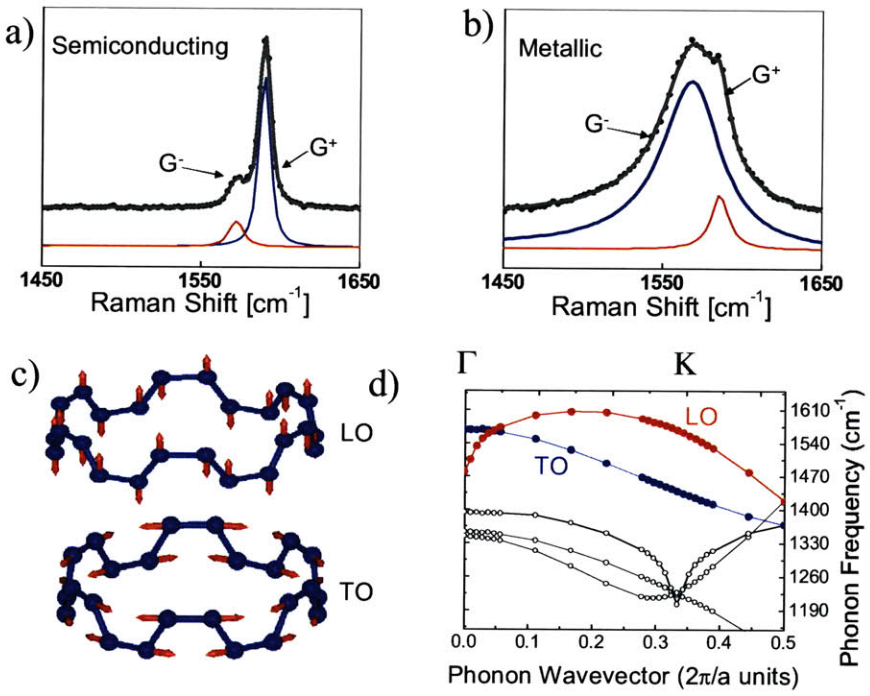

Figure 3-1: a) and b) G-band spectra of a semiconducting and a metallic carbon nanotube, respectively. c) the atomic displacements of the LO and TO modes [7]. d) the phonon dispersion of a metallic nanotube when showing a Kohn anomaly for the LO mode at the Γ-point [7]

3.1.1 The Kohn anomaly

The physical origin of the G-band lineshape of M-SWNTs has also been a debated topic. Several earlier works proposed that the broad and asymmetric lineshape of the G^- peak arises from a coupling between the TO mode and a low energy plasmon [10]. These theories were only able provide a qualitative explanation of the observed lineshape and its diameter dependence. Moreover, in order for the phonon-plasmon coupling satisfy the conservation of momentum, an extrinsic compensating momentum would to be provided by defects or bundling. This requirement contradicts the observation of the broadened feature in pristine isolate M-SWNTs [12]. In 2002 Dubay et al. [14] proposed that the LO mode is softened by a 'Peierls-like' mechanism, whereby the displacement of the phonon reduces the energy of the valence electrons in the vicinity of the Fermi level. Their result suggested that the lower energy G^- feature should be assigned to the softened LO mode rather than to the TO mode. Piscanec et al. [7] later calculated the phonon dispersion of M-SWNTs and found that there is a sharp kink in the phonon dispersion of the LO mode at the Γ point, which they refer to as a Kohn anomaly (KA) shown in Fig. 3-1 d). Both the Kohn anomaly and the 'Peierls like' mechanism describe the same physics of vibration that is softened by coupling to electrons near the Fermi surface.

Kohn anomalies occur for phonons whose displacements perturb the energy of the electrons at the Fermi surface. These electrons are able to rearrange themselves to screen the ions, thereby softening the vibration. The manifestation of the Kohn anomaly is a kink in the phonon dispersion at $q = 2k_F$. As the dimensionality of the system is reduced, the kink becomes more pronounced. In one dimensional systems, the kink becomes a logarithmic singularity due to Fermi surface nesting [15]. The Kohn anomaly is considered to be a precursor to a static 'Peierls distortion' which occurs when the frequency of the phonon is driven to zero [15].

3.1.2 Fermi level (E_F) dependence of the Kohn anomaly

Several works have calculated changes to the frequency and linewidth of the LO mode due to the Kohn anomaly. This was done by using second order perturbation theory to compute corrections to the phonon self energy. It has recently it has been shown [16, 17] that non-adiabatic effects, must be considered to fully capture the electron-phonon coupling in SWNTs. This is done by taking the energy of the phonon into account in the perturbation theory. The softening of the LO phonon frequency can be thought of as an energy renormalization due to the creation of intermediate virtual electron-hole pairs [16, 17] across the linear electronic bands. The resonant creation of a real electron-hole pair also leads to a lifetime broadening of the phonon. The corrections to the frequency and linewidth are computed by performing a sum over individual contribution of each e-h pair to the energy renormalization and lifetime broadening of the phonon.

As depicted in Fig. 3-2 a), changing the occupancy of the electronic bands will block electronic excitations with $E_{eh} < 2|E_F|$, thereby limiting the e-h which may contribute to the interaction. There shifting the Fermi energy away from the Fermi point will gradually suppress the energy renormalization and lifetime broadening of the phonon as more e-h excitation are Pauli blocked. The E_F dependence phonon frequencies in M-SWNT has been calculated in a number of works [16, 17, 6], however in this chapter we compare our work to the predictions of Sasaki et al. [17, 18, 6]. In Figs. 3-2 b) and c) we show the frequency and linewidth of LO phonon for a (10,10) M-SWNT. The blue curves are the predictions for $T = 0$ K and the red curves are for $T = 300$ K. The main features are 1) a broadening window $|E_F| < \hbar\omega_{LO}/2$ within which the LO phonon can decay into a real e-h pair and 2) two singularities in the frequency at $E_F = \pm\hbar\omega_{LO}$ which correspond to a resonance between LO phonon energy and the e-h energy of excitation from the Fermi surface.

In this chapter, we report on experiments in which we have tuned the Fermi level of M-SWNTs while measuring their Raman spectra. In the first half of the chapter we present results on the Fermi level dependence of the frequency, linewidth and lineshape

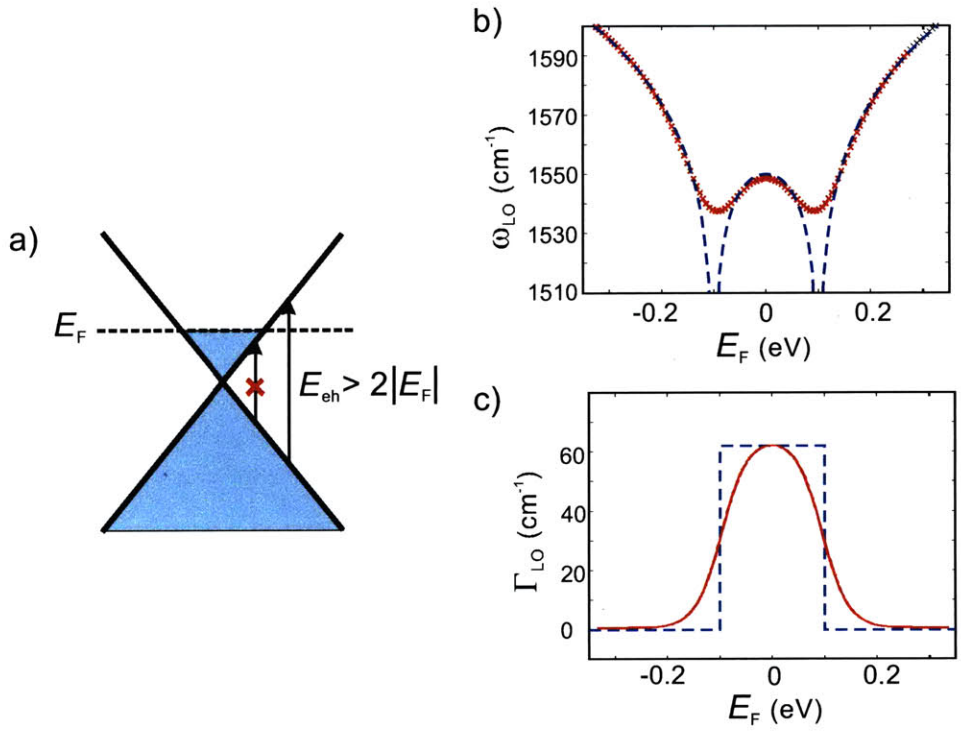

Figure 3-2: a) A schematic depicting virtual e-h pairs that contribute to the frequency renormalization and lifetime broadening of the LO phonon. Only e-h pairs satisfying $E_{\mathrm{e-h}} > 2\,|E_{\mathrm{F}}|$ may contribute. b) and c) The calculated frequency ω_{LO} and linewidth Γ_{LO} of the LO mode as a function of E_{F}. Calculations are taken from [6].

of the G-band. In the second part we extend this analysis to the radial breathing mode (RBM) which has also been predicted to be softened due to an interaction with e-h pairs [18].

3.2 Combined electrochemical gating and *in situ* Raman spectroscopy

We sought to modulate the Fermi level of individual M-SWNTs in a geometry that would permit us to simultaneously collect their Raman spectra. Being able to control the E_F using a gate voltage allows us to follow gradual changes in the Raman spectrum while keeping all other experimental conditions constant and without having to move the sample. In order to efficiently modulate E_F on both sides of the Dirac point, we used electrochemical gating to induce charge on the M-SWNTs. Electrochemical gating is able to achieve a very high gate efficiency by creating an electric double-layer capacitor at the interface between the nanotube and an electrolyte [19, 20]. Figure 3-3 a) is a schematic of the on-chip electrochemical cell that is used. SWNTs are grown, as described below, on a SiO_2/Si substrates, and subsequently, a 30nm Au ground electrode with a Cr adhesion layer was evaporated on half of the substrate to form, along with the nanotubes, the working electrode of the electrochemical cell. A transparent electrolyte is deposited on top of the nanotubes, and is contacted by a reference and a counter electrode see Fig. 3-3 a). In some of the earlier experiments, a simpler two electrode setup was used in the electrochemical cell.

3.2.1 Nanotube growth

Two different types of CVD growths were used for this study owing to the fact that the experiments took place over several years during which time growth methods were improved in our research group. In earlier experiments the SWNTs were randomly oriented and on the order of several to tens of microns long, whereas in later experiments, the aligned nanotubes were hundreds of microns long. In Fig. 3-3 b) and c)

we show an AFM image and an SEM image of the randomly oriented and aligned nanotubes, respectively. The randomly oriented SWNTs were grown using dispersed catalytic ferritin nanoparticles [21], and methane was used as the hydrocarbon source. The SWNT density was kept high enough to create a network of tubes that are connected to the ground electrode, but low enough to be able to observe spectra from individual tubes with a laser spot size of $\sim 1\mu$m. The long aligned nanotubes were grown using an $FeCl_3$ emulsion for the catalyst [22] and ethanol as the hydrocarbon source. There are several practical advantages to using aligned SWNTs, including the fact that the laser polarization can be aligned with all of the SWNTs on the sample, and the fact that nanotubes of interest can be located and returned to with a simple linear scan of the sample. After evaporating a Au electrode on half of the sample, all of the SWNTs are guaranteed to be contacted even hundreds of microns away from the electrode, while in the case of the randomly oriented nanotubes only those nanotubes in the immediate vicinity will be contacted.

3.2.2 Electrochemical cell

In order to get a high gating efficiency and stability at voltages greater than 1V, we used a molten polymer electrolyte similar to electrolytes used in Li ion batteries. The electrolyte recipe was adapted from [19, 20] where electrochemical gating was used to make nanotube field effect transistors. A 1:2 solution of $LiClO_4$ salt and polyethelyne oxide (3000MW) was used with methanol as a solvent which was evaporated off in an oven after the electrolyte was applied to the sample. The electrolyte absorbs little light in the visible light spectrum and has a Raman spectrum that does not interfere with the SWNT peaks of interest.

3.2.3 Raman spectroscopy

Raman spectra were taken in a backscattering geometry using a 100x objective to focus the M-SWNTs through the transparent electrolyte. A $\sim 1\mu$m laser spot was scanned along the edge of the ground electrode in search of M-SWNTs (based on the

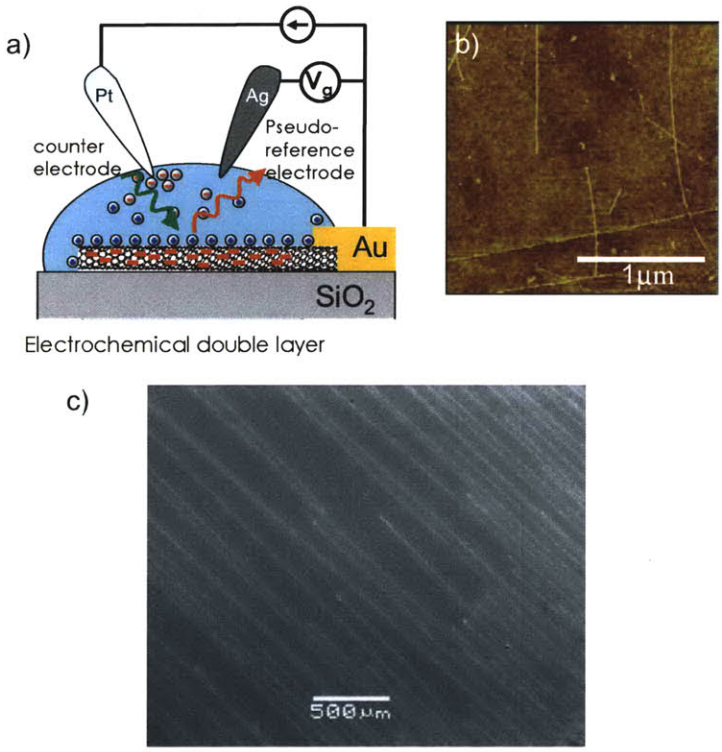

Figure 3-3: a) Schematic diagram of the experimental setup. The excitation laser shines through the PEO/$LiClO_4$ polymer electrolyte. b) An AFM image indicating that the nanotubes are spaced out and are typically isolated from one another. c) SEM image of long aligned SWNTS

radial breathing mode (RBM) frequency or the G-band lineshape). Once the desired SWNT was located, a series of spectra were taken, while sweeping the gate voltage. Raman modes of the electrolyte ($1450cm^{-1}$ and $1485cm^{-1}$) are also present in the spectral region of interest and can overlap with the tail of the broadened G-band. However, these peaks are independent of the applied gate voltage V_G and are easily distinguished from the G-band signal.

3.3 Softening of the G-band

Figure 3-4 a) is a representative map of the G-band intensity of a M-SWNT as a function of the gate potential V_G. Here we see a very drastic change in G^- frequency and lineshape as a function of gate voltage. The G^- peak shifts almost symmetrically about V_{G_o}=1.2V (Fig. 3-4 a) while the frequency of the G^+ peak remain constant low gate voltages, and upshifts only slightly at higher gate voltages. The gate voltage V_{g_o} corresponds to the charge neutrality point (i.e., the band crossing point), and its value is offset from zero, partly because of ambient doping from oxygen or perchlorate ions, and partly because, in this measurement, a reference electrode was not used. In later experiments, when using an Ag reference electrode, V_{g_o} is found to be much closer to zero.

The G-band spectra for the same nanotube, at each value of V_G, are shown in Fig. 3-4 b). Here we see that at V_{G_o}, the G^- peak has the lowest frequency ($1550cm^{-1}$) and amplitude, as well as the greatest full-width at half maximum (FWHM) ($68cm^{-1}$) linewidth. When the gate voltage is moved below or above V_{G_o}, the G^- peak frequency increases, its linewidth decreases, and the peak lineshape becomes increasingly similar to the G-band of S-SWNTs (Fig. 3-4 b).

In the above mentioned spectra, there are two distinct peaks whose evolution can be followed at each value of V_G. In general, the G-band of SWNTs band can contain up to six components corresponding to TO and LO phonon modes, each with either A, E_1 or E_2 symmetry [24]. The A symmetry modes typically make the largest contribution to the intensity [25] and therefore we assign the G^+ and G^- peaks

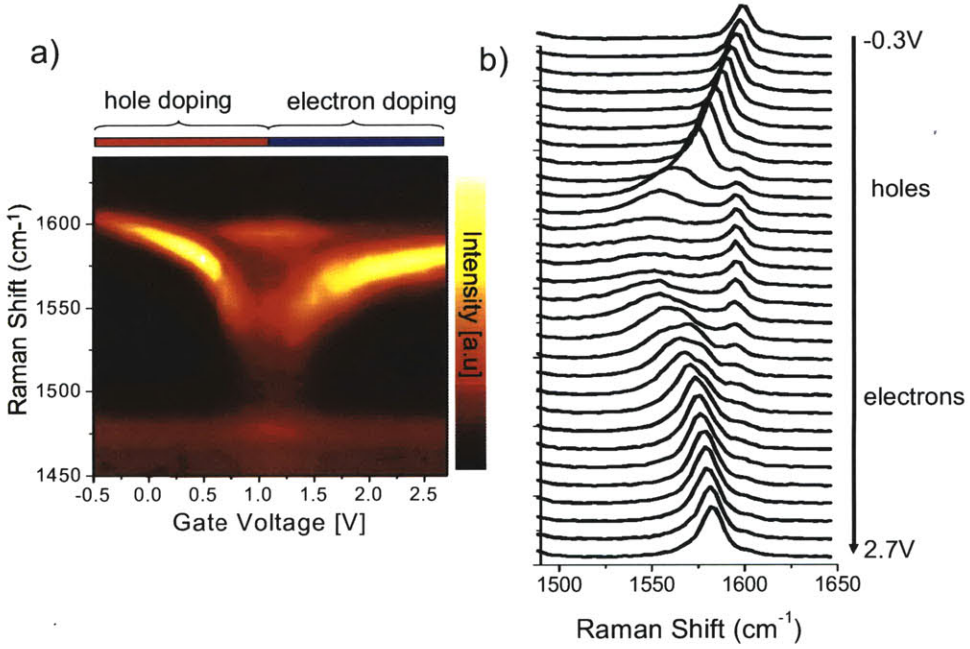

Figure 3-4: a) G-band intensity map vs. applied gate voltage V_G for an individual M-SWNT. b) G-band spectrum, for the same nanotube as in a), taken at the indicated V_G values. [23]

to the A-symmetry LO and TO modes, respectively. In some nanotubes, however, there are multiple overlapping peaks in the G-band spectrum, making it difficult to unambiguously fit the spectrum as a function of V_G [26]. Gaur et al. [27] show that extra peaks in the G-band of M-SWNT correlate with intensity of the disorder induced D-band. In our experiments we have focused M-SWNT with no appreciable D-band, and only two peaks in the G-band.

In Fig. 3-5 we show the V_G dependent spectra of a M-SWNT whose G-band is comprised of a single broad peak. This M-SWNT, excited at $E_{\mathrm{L}} = 2.33$ eV has an RBM frequency of 250 cm$-$1 and can therefore be assigned to a (12,0) zigzag M-SWNT. The TO mode is known to be absent in the Raman spectrum of zigzag nanotubes, which is consistent with the single broad peak that we observe in the G-band of this (12,0) tube. We fit the single peak using a BWF profile (3.1) and compare the V_G dependent frequencies and linewidths with those predicted by Sasaki et al. [17] using time dependent perturbations theory.

3.3.1 G-band linewidth as a function of E_{F}

The linewidth of the LO mode can be separated into a intrinsic term Γ_o and a gate dependent electron-phonon coupling term $\Gamma_{e-p}(V_G)$. The intrinsic linewidth, which includes contributions from phonon-phonon interactions and inhomogeneous broadening, is taken to be ~ 10 cm^{-1}. As a function of the Fermi level, Γ_{e-p} only contributes to the total linewidth within the broadening window defined by $|E_F| < \hbar\omega/2$. Within this window, the LO phonon is able to decay into an e-h pair of the same energy, and therefore its lifetime is decreased [28, 17]. At finite temperatures, the boundaries of the broadening window are smeared by the Fermi function. Figure 3-6 a) shows the experimentally determined linewidth of the (12,0) M-SWNT as a function of V_G, as determined from fitting the G-band to a BWF lineshape. On the same plot we have overlaid the theoretical prediction for the total linewidth $\Gamma_{LO} = \Gamma_{e-p}(V_G) + \Gamma_o$. By scaling the V_G, such that the width of the broadening window is set equal $\hbar\omega_{LO}$, we are able to estimate the gate efficiency as being $\alpha = 0.23$ eV/V. The magnitude of the broadening window, has not been scaled, and only depends the diameter the M-

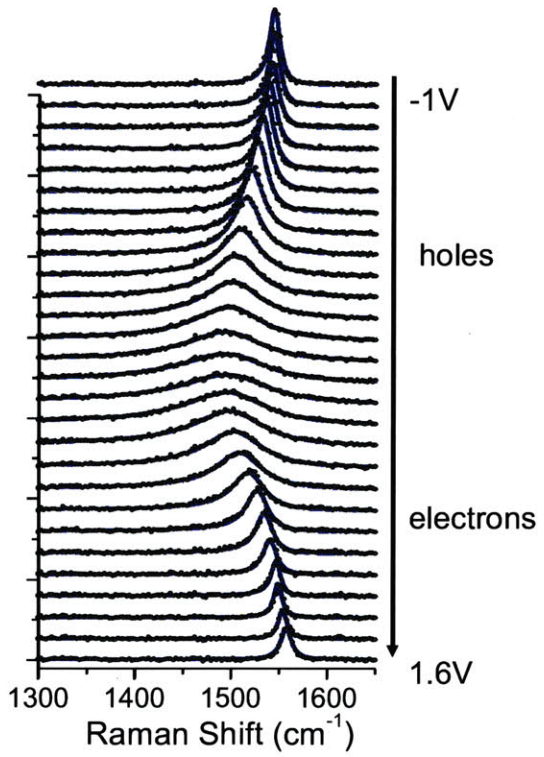

Figure 3-5: The G-band spectra of a (12,0) zigzag M-SWNT at various values of gate voltage V_G.

SWNT which was determined from its RBM frequency. The broadening window that we observe, is a signature of the nonadiabatic contribution to the Kohn anomaly. The quantitative agreement of the experimental linewidth is confirm that the nonadiabatic contributions to the phonon softening in M-SWNTs should not be neglected.

3.3.2 G-band frequency as a function of E_{F}

In Fig. 3-6 b), we plot the fitted frequencies of the LO mode as a function V_G overlaid with the predicted corrected frequency $\hbar\omega_{LO} = \hbar\omega_o + \hbar\omega_{e-p}$. We use the same E_{F} scale as for the linewidth and we have taken $omega_o$ to be 1610 cm^{-1}. Overall, the experimental frequency is in reasonable agreement with the predicted values, however we do not observe the two minima located at $\pm\hbar\omega_{LO}$. At $T = 0$, these minima develop into logarithmic singularities. The thermal distribution of carriers at room temperature smooths out these singularities, however the two minima should still be observable in a pristine nanotube, based on the calculation performed at $T = 300K$. Recently, these minima have been observed in very clean suspended M-SWNTs that were electrostatically gated [29]. We attribute the absence of these minima in our data to inhomogeneous charging from the electrolyte, as other charge inhomogeneities from the substrate.

The frequency of the LO mode is slightly asymmetric about $E_{\mathrm{F}} = 0$. We attribute this asymmetry to two possible mechanisms. Firstly, the gate efficiency α may not be equal on the hole doping and electron doping side, since different ions are participating in the charging of the nanotube. The second mechanism, is related to the change in the C-C bond length when the M-SWNT is charged. We expect the bond length to contract for hole doping and to expand for electron doping. This should result in higher frequencies for negative V_G than for positive V_G, as observed in Fig. 3-4 and Fig. 3-6. The doping induced change in bond length is discussed in greater detail in chapter 5.

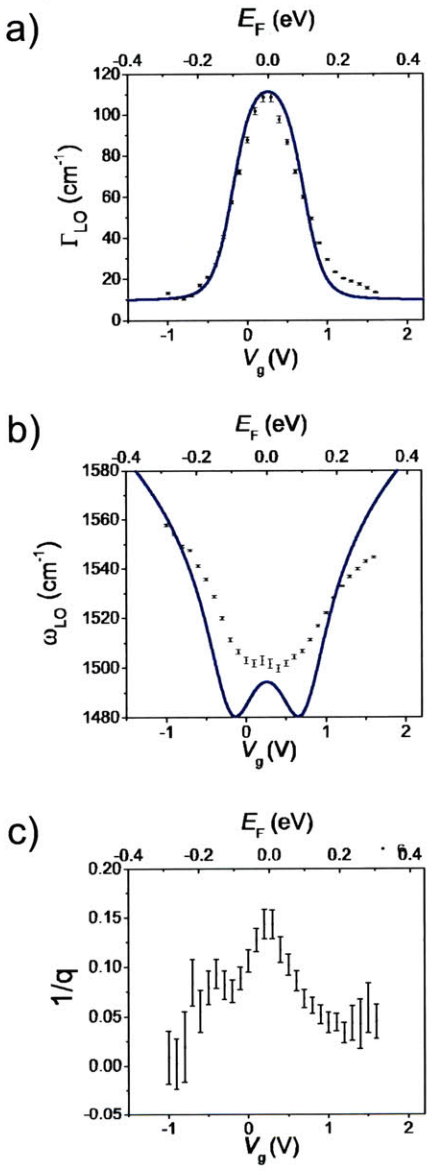

Figure 3-6: Comparison of the experimental frequency and linewidth of the G-band feature with theoretical predictions. The data points in a), b) and c) are the experimentally derived linewidths, frequencies and asymmetry parameters of the LO modes (12,0) M-SWNT shown in Fig. 3-5 as a function of the gate voltage. The solid curves in a) and b) are the predicted linewidth and frequency of a (12,0) M-SWNT. The calculations are adapted from [6].

3.3.3 Fano lineshape as a function of E_F

As mentioned above, we have fit the LO phonon lineshape with an asymmetric BWF profile (3.1. Figure 3-6 c) shows that the Fano factor $1/q$ decreases from 0.15 to 0 as the Fermi level is shifted away from the Fermi point. The change in $1/q$ appears follows the variation linewidth (Fig. 3-6 a), suggesting that the degree of asymmetry correlates with the strength of the e-p coupling. However, neither the asymmetry of the LO lineshape nor its E_F dependence, are predicted by the same e-p coupling mechanism that gives rise the E_F dependence of the LO frequency and linewidth.

It has been proposed that the Fano lineshape results from the interference between Raman scattering of the LO phonon and electronic Raman scattering from the continuum of electronic excitations [30]. In this scenario the Fano factor has a physical meaning which is given by $1/q = V_{e-p}M_p/M_e$ [30]. Here, V_{e-p} is the electron-phonon coupling matrix element and M_p and M_e are the Raman tensors for phonon and electron scattering, respectively. We expect the ratio M_p/M_e to depend on the (n,m) values of the nanotube. Since the phonon and electron Raman scattering processes have different resonance profiles, the ratio M_p/M_e is also likely to depend on E_L. This topic is addressed in detail in the next chapter where we describe the electronic contributions to the Raman spectrum of M-SWNTs.

3.3.4 Diameter dependence of the G-band phonon softening

Both the frequency renormalization and the linewidth broadening of the LO phonon are expected to increase with decreasing diameter, as $1/d_t$ [31, 17]. In Fig. 3-7 we show the intensity maps of G-band versus V_G for three M-SWNTs of different diameters that have been determined based on their RBM frequencies. Indeed, the smaller M-SWNT exhibit a stronger softening near their charge neutrality point. We have not collected a sufficient amount of data from (n, m) assigned M-SWNTs to comment on the chiral angle dependence of the LO phonon softening, however, the authors of [31, 17] do not predict any appreciable chirality dependence. On the other hand, Sasaki et al. [31, 17] do predict an interesting but mild E_F dependence of

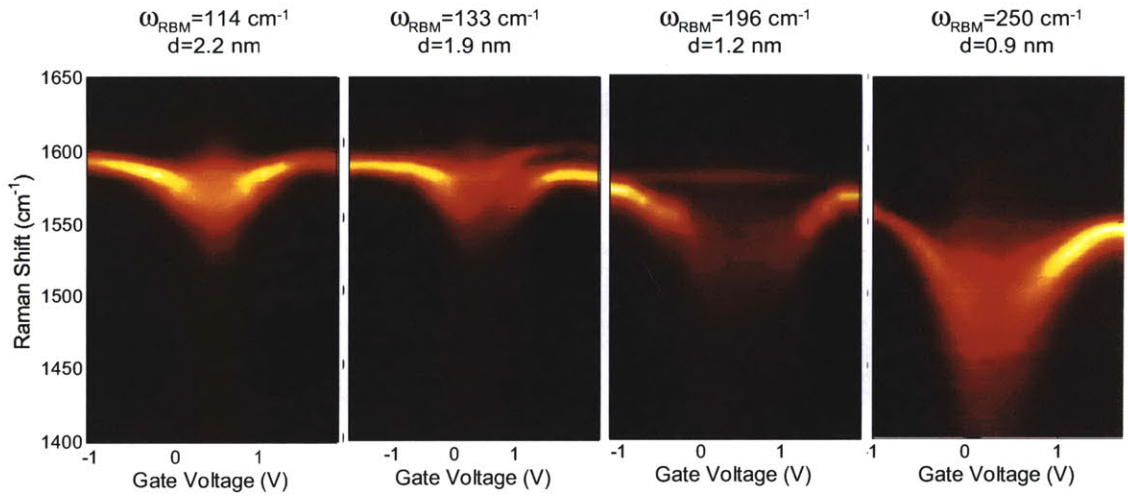

Figure 3-7: G-band intensity maps vs. applied gate voltage V_G for several M-SWNTs with different diameters. The diameters are estimated from the indicated RBM frequencies.

the TO mode. However, since the TO mode difficult to track because of its weak intensity, we have not yet found corroborating evidence for these predictions.

3.3.5 Summary of the G-band phonon softening

In this section we have studied the e-p coupling due to a KA in individual M-SWNTs by observing the evolution of the G-band Raman spectrum while applying an electrochemical gate voltage. In M-SWNTs where only two peaks are observed in the G-band spectra throughout the gating range, the peaks were unambiguously assigned and their behavior upon gating, in terms of frequency, linewidth and lineshape, was investigated. This data provides convincing evidence of the KA phenomenon in M-SWNTs and the experimental data are in good quantitative agreement with theoretical calculations [7]. A similar experiment was carried out previously [32], but clear evidence of a KA was not observed. This is most likely due to the presence of multiple peaks in the G-band.

3.4 Softening of the Radial Breathing Mode

Another phonon mode of interest in SWNTs is the isotropic radial deformation of the nanotube called the radial breathing mode (RBM). This optical phonon is solely the result of the one dimensional tubular structure of SWNTs and its deformations are very different from those of the optical stretching modes that are common to all other graphitic materials. Electron-phonon coupling of the RBM is important because it provides a new scattering channel for electrons that is absent in higher dimensional forms of carbon. Being a low energy optical phonon, the RBM could be a significant scatterer of low energy electrons such as in electrical transport at low biases [33].

A recent theoretical treatment of the E_F dependence of the RBM predicts a similar, albeit weaker, softening of the RBM phonon with a significantly larger chiral angle dependence [18]. Because the RBM energy is so much smaller than the G-band, the e-p coupling is expected to be much more sensitive to the fine structure of the electronic bands near the Dirac point where the valence and conduction bands touch. An experimental study of the softening of ω_{RBM} in M-SWNTs is therefore important to clarify the structure-dependent e-p coupling phenomena associated with the ω_{RBM} softening.

In this section we present a careful analysis of the frequency ω_{RBM} and linewidth Γ_{RBM} of the RBM of individual SWNTs as a function of the electrochemical gating potential V_G. We observe an increase in frequency when the nanotube is doped with either electrons or holes. Our experimental results show a diameter (d_t) and chiral angle (θ) dependence in the ω_{RBM} softening.

3.4.1 Radial breathing mode frequency as a function of E_F

Figure 3-8 a) shows the RBM spectrum of a M-SWNT at several values of V_G. A subtle upshift of 2 cm^{-1} for both ($\pm$) polarities of V_G is observed. Changes in ω_{RBM} are more evident after fitting the peaks, whereby the fit gives both ω_{RBM} and the FWHM linewidth Γ_{RBM} vs. V_G, shown in Figs. 3-8 b) and 3-8 c, respectively. We use a Voigt profile to deconvolute the instrumental broadening from the Lorentzian

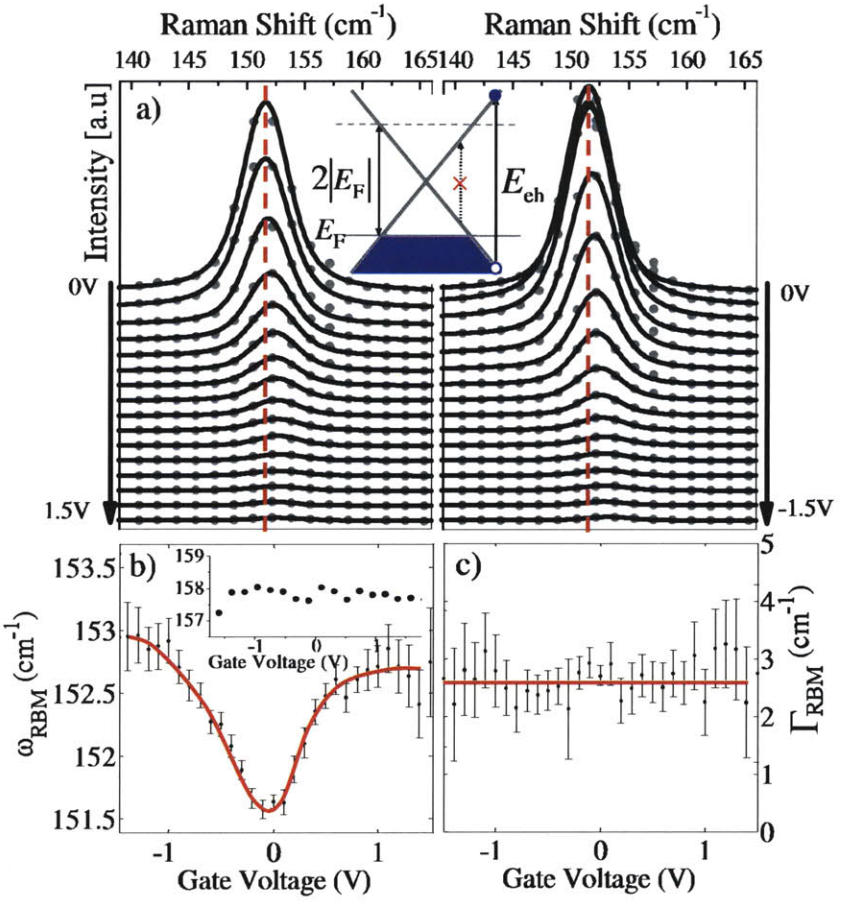

Figure 3-8: a)Waterfall plots of the RBM spectra of an M-SWNT at several positive (left panel) and negative (right panel) values of gate potential V_G. To evaluate the ω_{RBM} downshift we use the vertical red lines as fiduciary marks, indicating the peak frequency at $V_G = 0$. The inset of a) is a schematic band structure of a M-SWNT illustrating the allowed e-h transitions. b) Fitted frequency ω_{RBM} and c) linewidth Γ_{RBM} values vs. V_G. Error bars denote 95% confidence interval. Solid curves are a guide to the eye. The inset of b) shows the fitted $\omega_{\mathrm{RBM}}(V_G)$ for an S-SWNT [34].

linewidth of the RBM peak. The ω_{RBM} of the M-SWNT shown in Fig. 3-8 b) makes an almost symmetric "V" shape about $V_G = 0$. Previous studies suggest that environmental effects such as the van der Waals interaction with the substrate or surrounding solution may modify ω_{RBM} [35]. The latter effect presumably only contributes to a constant background with respect to V_G. The large drop in the peak intensity observed with increasing V_G may be caused by a change in the resonance condition. Because of the loss in peak intensity with increasing V_G, we are only able to follow $\omega_{\mathrm{RBM}}(V_G)$ for those M-SWNTs that have strong signals, which biases our sample set towards tubes with small θ values [18]. These M-SWNTs all exhibit a similar characteristic $\omega_{\mathrm{RBM}}(V_G)$ behavior. Meanwhile the RBM peak for an S-SWNT shows no appreciable change in $\omega_{\mathrm{RBM}}(V_G)$ as a function of V_G, as for example is shown in the inset of Fig. 3-8 b). It is thus clear that the behavior in Fig. 3-8 b) is an effect specific to M-SWNTs.

The behavior of ω_{RBM} for M-SWNTs can be understood by considering that, like the G-band phonons, the RBM is also an optical phonon capable of exciting vertical electron-hole (e-h) pairs across the linear k valence and conduction bands of the M-SWNT near the K (or K') point in the Brillouin zone. If the e-p matrix element for such transitions is non-zero, these scattering events contribute to renormalizing the phonon energy and decreasing its lifetime. As illustrated in the inset of Fig. 3-8, the Pauli exclusion principle limits the available e-h pair transitions to those satisfying $E_{\mathrm{e-h}} > 2\,|E_{\mathrm{F}}|$, thus giving rise to the V_G dependence of ω_{RBM}. As E_{F} is shifted away from the Dirac point, the number of excitations contributing to the *dressed* RBM phonon is reduced and ω_{RBM} approaches the frequency of the *bare* RBM phonon [18].

3.4.2 Radial breathing mode linewidth as a function of E_{F}

In Fig. 3-9 we compare the E_{F} dependence of the G^- peak (A_{LO} phonon) to ω_{RBM} of an M-SWNT which we tentatively assign as a (13,4) SWNT ($\omega_{\mathrm{RBM}} = 193$ cm^{-1}, $E_{\mathrm{Laser}} = 1.91$ eV). We see a striking resemblance between the V_G dependence of ω_{G^-} and that of ω_{RBM}, with both peaks displaying a minimum in frequency around $V_G = 0$. However, the Γ_{RBM} behavior of the two peaks is quite different, with the

RBM peak showing no noticeable broadening in contrast to the 60 cm^{-1} broadening of the G^- peak. The lack of broadening for the RBM indicates a negligible resonant decay of the RBM into an e-h pair.

To understand why the RBM is downshifted but not broadened, it is instructive to draw comparisons to the e-p coupling of the optical phonons that contribute to the G-band of graphene, M-SWNTs and S-SWNTs, which have recently been studied in great detail [36, 23, 26, 12, 37]. In M-SWNTs, the LO phonon (with energy 0.2 eV) is able to create real and virtual e-h pairs across the linear electronic bands, resulting in the strong broadening and downshift in frequency characteristic of the metallic G^- peak as shown in Fig. 3-9 Similarly, in graphene, the G-band phonons are both broadened and downshifted because they couple to e-h excitations near the Dirac point. In the case of S-SWNTs, the optical phonons do not have sufficient energy to excite e-h pairs excitations across the large electronic energy gap. However these optical phonons can still create virtual excitations which contribute to the downshift of the phonon frequency. Since there is no decay into real states, there is no linewidth broadening and the frequency shift is modest compared to M-SWNTs, as recently verified in experiments [38, 37].

Since $\hbar\omega_{\mathrm{RBM}}$ is a small fraction of the LO/TO phonon energies, the e-h excitations for the RBM occur much closer to the Dirac point. On this energy scale, a very small energy gap such as the curvature-induced minigap, becomes significant. The latter, given by $E_{\mathrm{gap}} = (A/d_{\mathrm{t}}^2)\cos(3\theta)$, is greatest for zigzag M-SWNTs and absent for armchair M-SWNTs. The value of A is about 60 meV based on an extended tight-binding model [18]. From the perspective of the RBM phonon, the electronic bands of small diameter zigzag M-SWNTs with $E_{\mathrm{gap}} > \hbar\omega_{\mathrm{RBM}}$ appear semiconducting-like. Only the armchair SWNTs have truly metallic bands when close to the Dirac point. Indeed, for the (13,4) SWNT shown in Fig. 3-9, $E_{\mathrm{gap}} = 32$ meV ($d_{\mathrm{t}} = 1.2$ nm, $\theta = 13^\circ$) exceeds $\hbar\omega_{\mathrm{RBM}}$ (24 meV) and hence no linewidth broadening is expected.

In Fig. 3-10 we show ω_{RBM} vs. E_F for the (13,4) nanotube calculated from the effective mass theory in [18], which also predicts no change in Γ_{RBM} as a function of E_{F} and a ω_{RBM} behavior qualitatively similar to what we observe in our measurements.

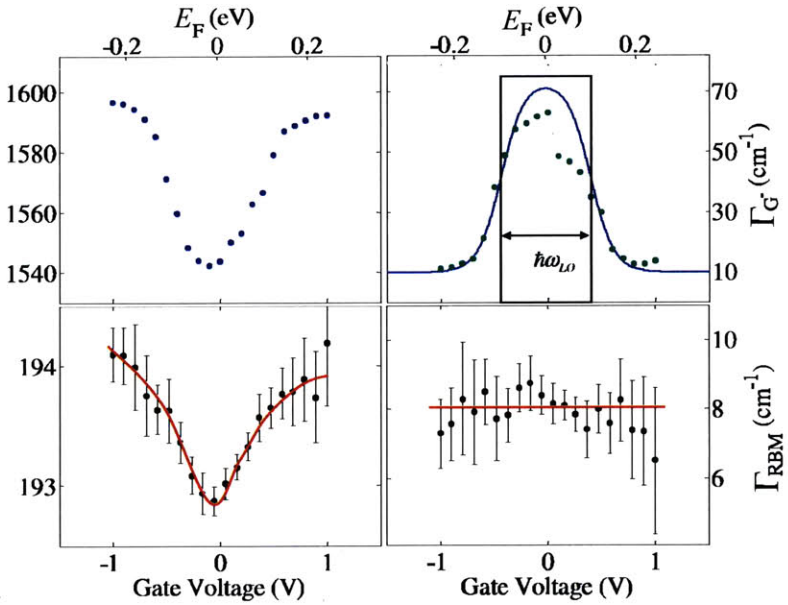

Figure 3-9: Comparing the G^- and RBM peaks vs. V_G for a (13,4) M-SWNT ($\omega_{\mathrm{RBM}} \sim$ 193 cm^{-1}, E_{laser} = 1.91 eV). a) G^- frequency and b) G^- linewidth vs. V_G (bottom axis) and E_F (top axis). The V_G dependence of the Γ_{G^-} is used to estimate the gating efficiency, $\alpha = 0.24$ eV/V. The box in b) gives the T=0 energy range within which the LO phonon can excite real e-h pairs. c) ω_{RBM} and d) Γ_{RBM} vs. V_G for one M-SWNT [34].

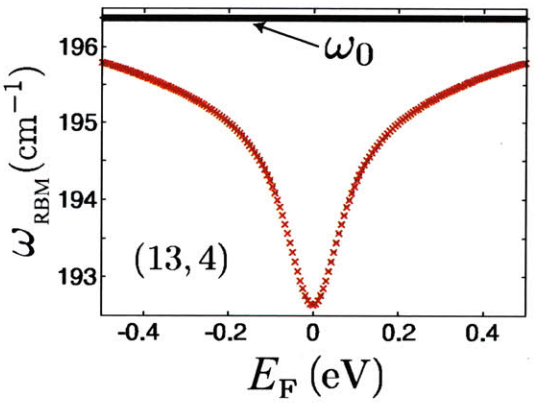

Figure 3-10: Calculated ω_{RBM} for a (13.4) M-SWNT vs. E_{F}. For this M-SWNT the e-p coupling contribution to the Γ_{RBM} is zero. Black points ω_0 give the *bare* ω_{RBM} and red points gives ω_{RBM} corrected for e-p related softening [18].

For a quantitative comparison, we converted the V_G scale of Fig. 3-9 to an energy scale (bottom axis) using a gate efficiency of $\alpha = 0.24$ (eV/V). The α value is determined by fitting the broadening window of the G^- peak to: $\Gamma_{G\_} = \Gamma_o + \Gamma_{e-p}(V_G)$, as shown in Fig. 3-9 b). Here, Γ_{e-p}, the linewidth due to e-p coupling is given by equation (29) of [39]. The V_G independent contributions to the linewidth are included in Γ_o which is taken as 10 cm^{-1} based on our experimental results. Comparing Fig. 3-9 c) with Fig. 3-10 within the same E_{F} range, we see that the experimental shift of ω_{RBM} is approximately a factor of 2 smaller than that predicted.

3.4.3 Diameter dependence of the RBM softening

It is important to know in what d_{t} range the softening of ω_{RBM} becomes significant. The downshift in ω_{RBM} is greatest in smaller d_{t} M-SWNTs as seen in Fig. 3-11, which plots of the observed frequency downshift of ω_{RBM} relative to $V_G = V_0 + 1V$ (black) and relative to $V_G = V_0 - 1V$ (red) as a function of $1/d_{\mathrm{t}}$ for several M-SWNTs, where V_0 is the gate voltage where the minimum in frequency occurs. The e-p matrix element and hence the frequency shift $\Delta\omega_{\mathrm{RBM}}$ at a constant V_G is expected to be linear in $1/d_{\mathrm{t}}$ [18]. The experimental data for $\Delta\omega_{RBM}$ increases monotonically vs. $1/d_{\mathrm{t}}$ with some variation that we attribute to the expected θ dependence of ω_{RBM}

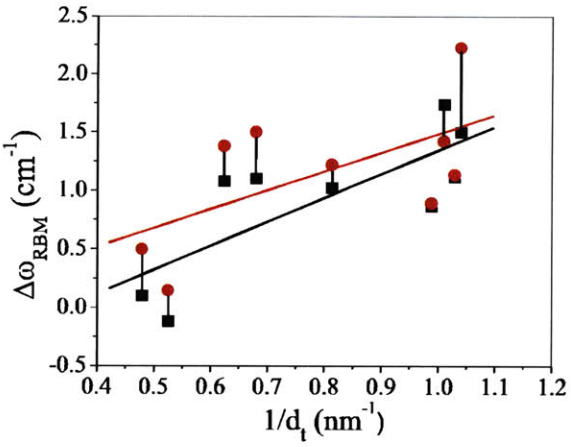

Figure 3-11: Downshift $\Delta\omega_{\mathrm{RBM}}$ in ω_{RBM} vs. $1/d_t$. Red circles indicate the shift relative to $V_G = V_0 - 1V$ (hole doping) and black squares the shift relative to $V_G = V_0 + 1V$ (electron doping). Solid lines represent linear fits to the data points [34].

[18]. Note that the shift on the negative gate side is in most cases greater than it is on the positive side. We attribute the mild asymmetry with respect to the sign of V_G to the C-C bond softening (stiffening) due to charging the lattice with electrons (holes). This topic is addressed in Chapter 5. There may also be a difference in the gating efficiency for $\pm V_G$.

3.4.4 Chiral-angle dependence of the RBM softening

To further explore the θ dependence of ω_{RBM} we have measured the V_G dependence of three consecutive M-SWNTs from the $2n + m = 24$ family, namely (11,2), (10,4), and (9,6) as shown in Fig 3-12. For a given V_G, the magnitude of the measured $\Delta\omega_{\mathrm{RBM}}$ decreases from the (11,2) to the (9,6) nanotube. This is in agreement with the predicted θ dependence of the downshift in ω_{RBM} [18]. The e-p matrix element, given approximately by $\langle \text{e-h}|H_{\mathrm{ep}}|\text{RBM}\rangle = g(|s_z|/d_t)\cos(3\theta)$, where g is the on site e-p coupling constant and s_z is the radial displacement, is greatest for the zigzag M-SWNT and approaches zero for the armchair M-SWNT [18]. Consequently the zigzag RBM is expected to exhibit the largest frequency shift but no broadening, while the armchair RBM should show neither a change in ω_{RBM} nor in Γ_{RBM}. An M-SWNT with an intermediate chiral could be expected to exhibit both a frequency

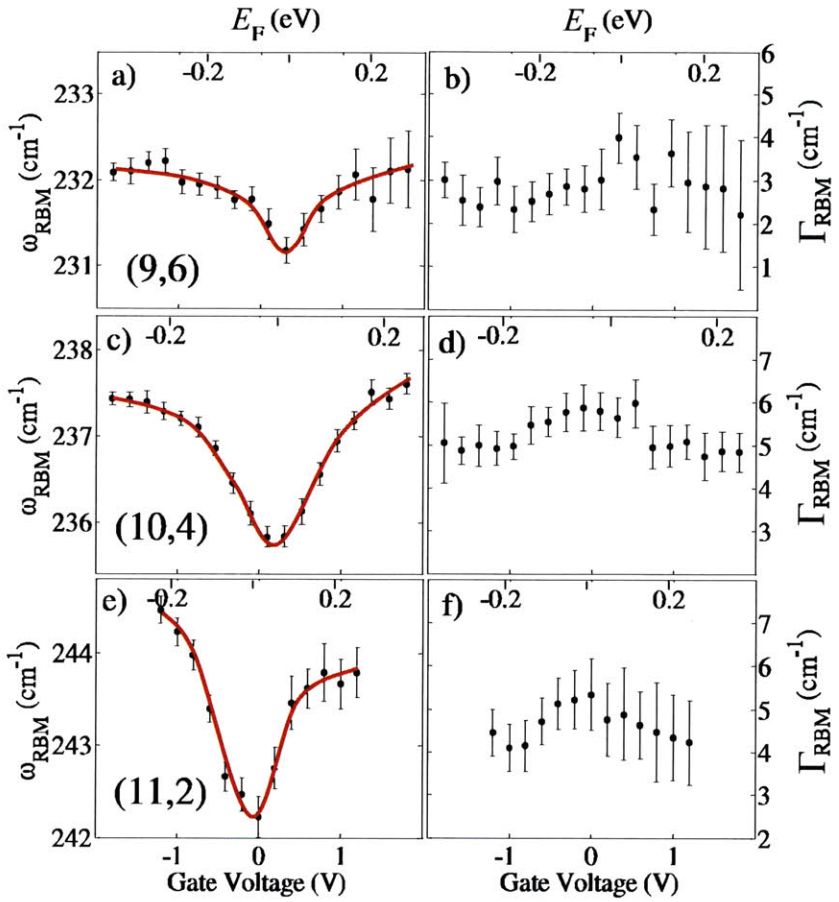

Figure 3-12: Fitted ω_{RBM} and Γ_{RBM} vs. V_G for three M-SWNTs from family $2n+m=24$. a) and b) (9,6); c) and d) (10,4); e) and f) (11,2). The curvature-induced energy gaps for the three M-SWNTs are 19.3, 41.7 and 60.5 meV, respectively. The energy scale (top axis) is estimated for each M-SWNT as in Fig. 3-9. Solid red lines are curves to guide the eye [34].

shift and a broadening. Within the $2n+m=24$ family, only the (9,6) and (8,8) tubes have an RBM phonon which is greater in energy than the curvature-induced bandgap. As shown in Ref. [18], the (9,6) tube is expected to exhibit a broadening $\Delta\Gamma = 2$ cm^{-1} and a negligible frequency shift at 300K. However, we observe a small frequency shift and no change in linewidth. On the other hand, the (10,4) SWNT is not expected to exhibit any broadening, but we observe a possible small broadening of $\Delta\Gamma = 1$ cm^{-1}. Besides these deviations, the overall measured d_t and θ dependences of the ω_{RBM} downshift are in good qualitative agreement the predictions of Ref. [18].

3.4.5 Evidence of small gaps in M-SWNTs

It should be noted that the energy gaps for the (9,6) and (10,4) nanotubes are only 7 meV below and 15 meV above their RBM phonon energies, respectively. The ω_{RBM} and Γ_{RBM} of M-SWNTs are predicted to depend strongly on the position of the cutting line with respect to the K point, as well as on the size of the energy gap with respect to the $\hbar\omega_{\mathrm{RBM}}$. Small perturbations to the lattice such as caused by strain [40], the displacement of the A_{LO} phonon [14, 41], and breaking of mirror symmetry [42] could sufficiently change the electronic structure to alter the E_{F} dependence of the RBM peak.

3.4.6 Summary of RBM softening

In this section we have experimentally confirmed that there is a mild softening of the ω_{RBM} of M-SWNTs which can be removed by both positive and negative doping. The magnitude of the downshift scales with $1/d_{\mathrm{t}}$, and is largest for small θ. The measured ω_{RBM} shifts agree qualitatively with the curvature-dependent softening predicted in Ref. [18]. No gate-induced change in Γ_{RBM} is found for most of the SWNTs that we studied, as is expected [18] for small (d_{t}) SWNTs. Our result shows that chirality dependent corrections to ω_{RBM} are required to better assign the d_{t} and (n, m) indices for small d_{t} M-SWNTs, and that environmental doping can be responsible for some of the variability in the observed ω_{RBM} behavior. This work also implies that the role of the RBM in electrical transport and other phonon assisted relaxation processes warrants further investigation.

3.5 Summary

In this chapter report our studies of the interaction of the G-band and RBM phonons of metallic SWNTs with intraband electron-hole pairs. We followed the frequency and linewidth of these phonons as a function of the Fermi level which was modulated using an electrochemical gate. The the experimentally observed G-band frequency

and linewidth behavior as a function of E_F is in good agreement with the theory of the Kohn anomaly. In particular the broadening window that we observed within $\pm\hbar\omega/2$ is a direct indication that non-adiabatic effects must be accounted for. The frequency of the RBM is also found to be softened due an interaction with virtual electron-hole pairs. However that lack of broadening for the RBM mode is an indication that in all the nanotubes that we have studied there exists an insulating bandgap greater than the RBM energy. This is important in light of recent reports of a Mott insulating state in metallic nanotubes [43], that show that even nanotubes that do not have a curvature-induced bandgap exhibit a small gap due to electron correlations.

Chapter 4

Resonant Electronic Raman Scattering

In this chapter we present a new feature in the Raman spectrum of metallic carbon nanotubes that we attribute to *electronic* inelastic light scattering by interband electron hole pairs. In chapter 3, we discussed how low energy electron-hole pairs contribute to the renormalization and lifetime broadening of optical phonons in metallic nanotubes. Here, we show that these same interband electron hole excitations can scatter light via the Coulomb interaction, giving rise and *electronic* Raman spectrum. The electronic Raman scattering (ERS) feature is found exclusively in the Raman spectrum of metallic nanotubes. The ERS spectrum exhibits broad peaks that appear at a constant photon energy due to a resonance of the scattered photons with the optical transition energies of the metallic nanotube. Our results are consistent with the picture that the mild asymmetry in the lineshape of the G-band Raman feature is the result of an interference between the overlapping ERS and vibrational Raman scattering by the LO phonon mode.

4.1 Background

Inelastic light (Raman) scattering is a versatile tool for studying elementary excitations in condensed matter systems. Electronic Raman scattering, which occurs when

the scatterer is a single or collective electronic excitation, has provided insightful information about electrons in low dimensional semiconductors [44] and in correlated electron systems [45]. Metallic single-walled carbon nanotubes ($M-$SWNTs) have emerged as a uniquely pristine medium for studying electrons and their correlations in one dimension [43]. However, despite the large impact of vibrational Raman spectroscopy in the area of carbon nanotube research, light scattering by electronic excitations has not yet been observed in the Raman spectrum of carbon nanotubes.

In this chapter we show the first experimental measurement of the electronic contributions to the Raman spectrum of individual metallic carbon nanotubes. Incident photons lose part of their energy to electrons excited across the linear electronic subbands of $M-$SWNTs. These scattering events are only detectable when they resonant enhanced. This occurs when either the incoming or outgoing photons match one of the optical transition energies of the M-SWNT (M_{ii}). Electronic Raman scattering is, therefore, a manifestation of the Coulomb coupling between electrons in the linear electronic bands of $M-$SWNTs, that determine their transport properties, and the higher electronic bands that determine their optical properties.

4.2 Experiments on M-SWNT of known (n, m) indices

In order to demonstrate that the Raman peaks which we attribute to ERS are intrinsic features of individual metallic SWNTs, we have focused on SWNTs, whose (n, m) indices have been identified by means of Rayleigh scattering spectroscopy [46, 47, 12]. The Rayleigh scattering spectrum maps out the VHSs in the DOS of a SWNT, and can therefore can be used to identify its optical transition energies. Combined with the RBM frequency obtained from Raman spectroscopy, this method can be used to unambiguously identify the structure of any given SWNT. Moreover, the presence of more than a single nanotube is immediately evident in the Rayleigh spectrum. Therefore Rayleigh scattering serves as a excellent method for identifying isolated

SWNTs.

Rayleigh scattering was performed using a white light supercontinuum laser source. Two objective lenses oriented at a 90° angle to each other are used to focus the white light spectrum onto the nanotube and to collect the scattered photons which are then focused onto a spectrometer. The SWNT that we have studied were grown over slits that were etched through a silicon wafer. To make the these slits, we start with a 500 μm thick Si wafer that is coated with a 50nm thick layer of Si_xN_{1-x} deposited by low pressure chemical vapor deposition. Using optical lithography, followed by reactive ion etching (RIE) the trench pattern is transfered to the Si_xN_{1-x} layer, on the backside of the wafer, which acts as an etch mask for the Si. A KOH solution is used to wet etch all the way through the Si substrate resulting in $15 - 50$ μm features on the front side of the wafer. The remaining Si_xN_{1-x} mask is etched off and the sample is then annealed in air in order to grow a thin SiO_2 layer. Long aligned carbon nanotubes are then grown across the trenches by chemical vapor deposition as described in chapter 3.

4.3 The Electronic Raman Scattering (ERS) feature

In Fig. 4-1, we compare the Raman spectrum of an $M-$SWNT and an $S-$SWNT whose optical transition energies (M_{11}) and structural parameters (n, m) were thus identified. For the $M-$SWNT, the two Rayleigh peaks in Fig. 4-1a correspond to energies of the second optical transition split by the trigonal warping effect ($M_{22}^{+} = 2.19$ eV, $M_{22}^{-} = 2.08$ eV) [47, 12], while in the case of the $S-$SWNT, the two peaks in Fig. 4-1b correspond to the third and fourth optical transitions with $S_{33} = 1.66\ eV$ and $S_{44} = 1.84\ eV$. A clear exciton-phonon sideband is visible at ≈ 200 meV above the S_{44} transition, confirming that it is an $S-$SWNT [46]. The absence of other Rayleigh peaks in this energy range is a clear indication that these nanotubes are isolated. The energy and splitting of the Rayleigh peaks along with the measured

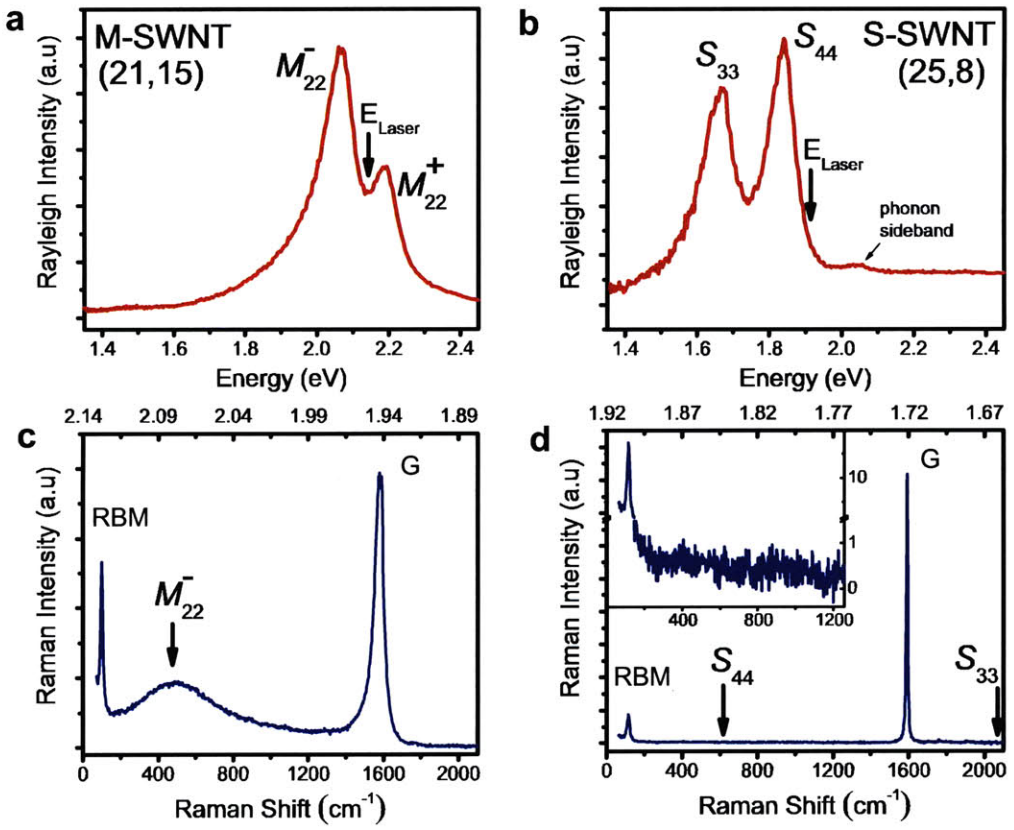

Figure 4-1: Comparing the spectra of a metallic (left) and a semiconducting nanotube (right). The Rayleigh scattering spectra a) and b) are used to identify the (n, m) of an isolated $M-$SWNT in a) and $S-$SWNT in b). Labels indicate the positions of the optical transitions. c) and d) are the corresponding Raman spectra with the Raman shift indicated on the lower axis and the energy of the scattered photon indicated on the top axis. Arrows indicate the energies of the optical transitions obtained from the Rayleigh spectra. Likewise, the Raman excitation energies are indicated with arrows in a) and b). The inset of d) shows the weak featureless tail in the Raman spectrum of the $S-$SWNT in b).

radial breathing mode peak frequencies (RBM) of around 100 cm^{-1}, and 115 cm^{-1} allow us to assign these to a (21,15) $M-$SWNT and a (25,8) $S-$SWNT, respectively. The broad and asymmetric G-band lineshape in Fig. 4-1 c) near $\sim$1580cm^{-1} further confirms the metallic nature of this SWNT.

The feature of particular interest in the Raman spectrum in Fig. 4-1 c) is the broad peak located at $\sim$504 cm^{-1}, in between the G-band feature and the RBM. This peak is symmetric and has a full width at half maximum (FWHM) of $\sim$ 620 cm^{-1}(77 meV). Conversely, there is no appreciable background signal in the spectrum of the $S-$SWNT shown in Fig. 4-1 d), which was also excited just above resonance (1.91 eV). A background spectrum was collected and subtracted from the signal such that there are no contributions from stray light or dark current in the spectra shown in Fig. 4-1. Interestingly, the scattered photon energy of the new feature in Fig. 4-1 c) matches the position of the M_{22}^{-} transition.

4.4 Resonant Electronic Raman Scattering

Tuning the laser energy, E_{L}, reveals that the Raman frequency of this new feature is highly dispersive. Figure 4-2 a) shows the spectra obtained at various incident laser energies as a function of the energy of the scattered photon. Although the Raman frequency of the ERS feature changes with E_{L}, the energy of the Raman scattered photons, E_S, remains centered around 2.08eV for E_{L} in the range 2.10 eV to 2.20 eV, and around 2.19eV for E_{L} = 2.33 eV. These values of E_S match the M_{22}^{-} and M_{22}^{+} energies from the Rayleigh spectrum, respectively. The same behavior is shown in Fig. 4-2 b) for a structure-assigned (27,9) $M-$SWNT of similar diameter but of smaller chiral angle, as indicated by the larger splitting of the M_{22}^{+} and M_{22}^{-} peaks [5]. We have consistently observed an ERS feature whose photon energy matches M_{22} for a collection of more than 15 structure-assigned $M-$SWNTs.

The M_{11} or M_{22} transitions of several other isolated $M-$SWNTs, both suspended and also on an SiO_2 substrate, have been determined from the RBM resonance Raman window [49]. Again, we systematically observe a broad feature at the energy of the

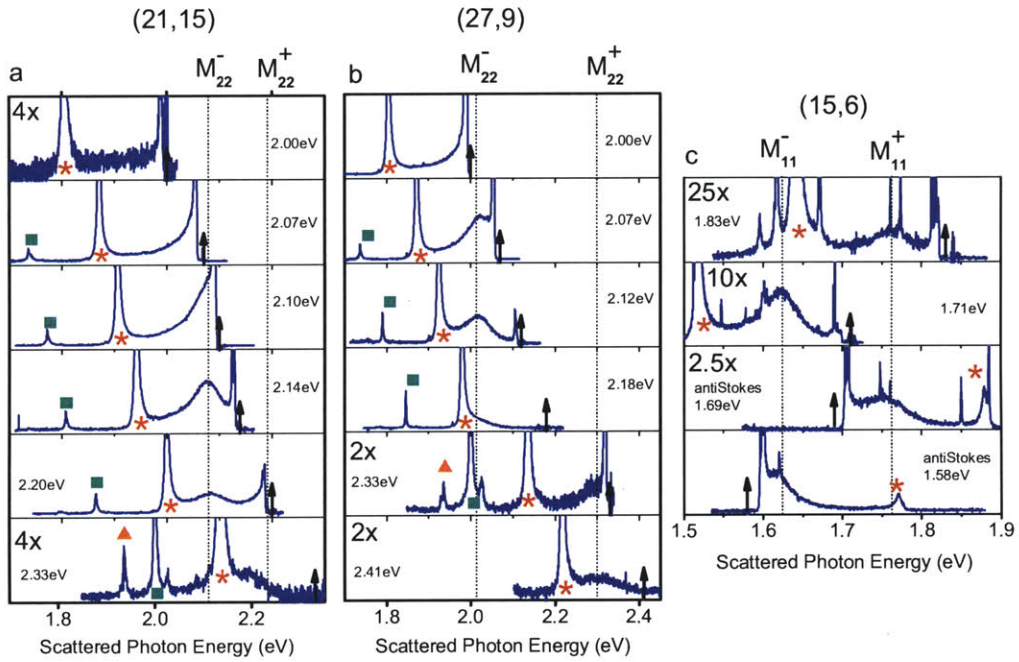

Figure 4-2: Following the ERS feature as a function of laser energy. a) Raman spectra of the (21,15) $M-$SWNT from Fig. 4-1 a), c) at several different excitation energies indicated here by the black arrows. The bottom axis is the energy of the Raman scattered photon. The dotted vertical lines indicate the energies of the M_{22} transitions as obtained from fitting the Rayleigh scattering spectrum using an excitonic model [46]. The asterisk, square and triangular markers indicate the positions of the G-band, G'-band and 2D'-band features, respectively [48]. All spectra are normalized to the G-band intensity. b) Same as a) but for a (27,9) isolated $M-$SWNT. c) Spectra from a $M-$SWNT on a substrate (not identified by Rayleigh). Here the ERS feature is shown for the M_{11} peaks and appears on both the Stokes and anti-Stokes spectra. From the RBM frequency and the position of the ERS peaks we assign this $M-$SWNT as (15,6).

M_{ii} transitions, when E_{L} is near M_{ii}. Finally, the ERS feature is also present in the anti-Stokes spectrum when an $M-$SWNT is excited slightly below resonance (Fig. 4-2 c). On the other hand, the Raman background of more than 15 structure-assigned $S-$SWNT excited near their S_{ii} transitions is nearly flat, with the exception of a weak tail near the Rayleigh peak, as shown in the inset of Fig. 4-1 d). Based on this survey of a statistically significant number of individual tubes, we conclude that the newly observed feature is a hallmark of $M-$SWNTs and can be observed for any $M-$SWNT excited near resonance.

We here attribute the observed peaks to a resonant electronic Raman scattering process, involving low-energy electronic transitions across the linear bands of $M-$SWNTs. Figure 4-3 shows a schematic diagram of the resonant ERS process. A continuous range of available electronic excitations may scatter light. While the density of states of these excitations is constant [1], the ERS events that result in outgoing photons of the same energy as one of the M_{ii} transitions will be resonantly enhanced and will dominate the signal. Consequently, the ERS feature is always centered at M_{ii}, irrespective of E_{L}. The strong but featureless tails observed when an $M-$SWNT is excited very close to a resonance (Fig. 4-2) involve very low energy e-h pairs. As E_{L} is tuned further away from a M_{ii} resonance, higher energy e-h pairs will contribute and a well defined ERS peak will develop at a Raman frequency corresponding to the laser detuning frequency. The energy of the scattered photons, however remains unchanged.

In this picture, the ERS spectrum is composed of contributions from many e-h excitations, whose relative amplitudes are modulated by the nearest M_{ii} resonance. The linewidth is then expected to be a sum of the M_{ii} width, γ_{ii}, and the spectral width γ_{eh} of the pertinent e-h excitations. In our experiments $\gamma_{ii} \approx 100$ meV, while time-resolved photo-emission measurements suggest $\gamma_{eh} < 10$ fs [50]. Since $\gamma_{eh} << \gamma_{ii}$, we expect similar widths for both the ERS and Rayleigh scattering features. Experimentally, we find that the widths of the observed ERS features tend to be slightly narrower, but of the same order of magnitude, as the associated M_{ii} transition.

The fact that the new ERS features are observed exclusively at M_{ii} in $M-$SWNTs,

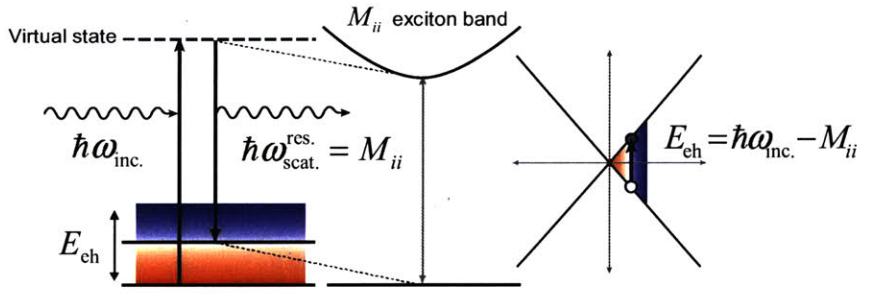

Figure 4-3: Schematic of resonantly enhanced electronic Raman scattering in an armchair $M-$SWNT. There is a continuum of e-h excitations to scatter by (illustrated by the gradient). The downward arrow indicates the resonantly enhanced scattering event, whose outgoing energy matches the M_{ii} optical transition energy (shown on right).

and not in $S-$SWNTs, together with the presence of the ERS features both on the Stokes- and anti-Stokes sides of the spectra, rules out fluorescence as a possible interpretation. Stokes-fluorescence from $M-$SWNTs or from higher-order transitions ($S_{ii}, i > 1$) in $S-$SWNTs is extremely inefficient because the exciton radiative decay rate in SWNTs ($\approx 0.1\text{ns}^{-1}$ [51, 52, 53]) is at least five orders of magnitude slower than non-radiative interband relaxation processes [54, 55, 50]. Anti-Stokes fluorescence would require additional phonon-assisted processes, which are even less likely to occur. Also, in a fluorescence scenario, we would expect to observe visible emission from both $M-$SWNT *and* $S-$SWNT, in obvious contradiction with our results.

4.5 Gate-voltage dependence of the ERS feature

Supposing that low-energy electronic excitations are responsible for the observed ERS, then by changing the occupancy of the electronic states, we should be able to suppress these features. Figure 4-4 shows the evolution of the Raman spectrum of an $M-$SWNT on an SiO_2 substrate whose Fermi level, E_F, is tuned by means of an electrochemical gate [23]. The ERS feature diminishes in intensity when the Fermi

level is shifted to positive or negative values. This further demonstrates that the e-h excitations are responsible for the ERS peak and also that small levels of doping (< 0.005 e/C atom) will suppress the ERS peak. In Fig. 4-4 c) and d), we also notice that the quenching of the ERS signal is accompanied by a strong narrowing and stiffening of the G-band feature. The latter two observations have been well documented [23, 12, 37, 26], and were attributed to the coupling of optical phonons and e-h pairs of similar energy.

4.6 Coupling of the ERS and G-band feature

In $M-$SWNTs the higher and lower frequency components of the G-band (G^+ and G^-) [56], are associated with the transverse optical (TO) and longitudinal optical (LO) phonon modes, respectively. As discussed in chapter 3, the LO mode is known to be broadened and downshifted because of its interaction with low lying e-h pairs [37, 57, 23, 12]. This mode has also been reported to be skewed toward lower wavenumbers, however the magnitude and the origin of this asymmetry in the lineshape remain debated topics [10, 13, 11, 12]. Typically the Breit-Wigner-Fano lineshape introduced in chapter 3 (equation 3.1),

$$I_{LO}(\omega) = I_o \frac{[(q \cdot \Gamma_{LO} + (\omega - \omega_{LO}))]^2}{(\omega - \omega_{LO})^2 + \Gamma_{LO}^2},$$

is used to fit the LO phonon peak. Here, I_o is a constant and the Fano factor $1/q$ is a measure of the asymmetry of the Raman peak, with a Lorentzian lineshape being recovered when $1/q \rightarrow 0$. In light of the recent discussion surrounding the lineshape of the G-band [10, 13, 11, 12], it is important to distinguish the LO phonon contribution to the Raman spectrum from the broad ERS background with which it often overlaps. In particular, we ask whether the asymmetry of the G-band lineshape is present once the ERS background has been accounted for.

As shown in Fig. 4-2, when present, the ERS feature only appears between the laser line and the G-band feature. The ERS feature is most prominent when it is

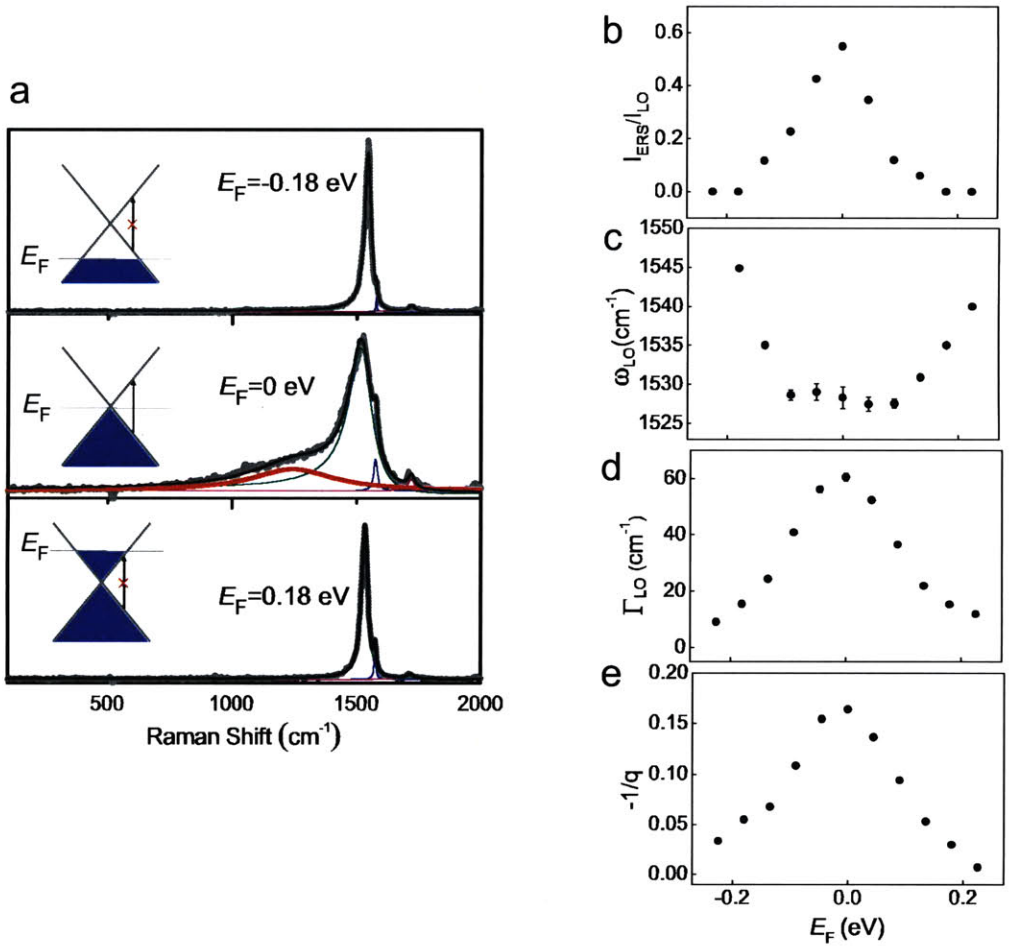

Figure 4-4: Quenching the ERS feature by Pauli blocking electronic excitations. a) The Raman spectra of an electrochemically gated $M-$SWNT. The ERS peak shown by the bold red line is suppressed when the Fermi energy, E_F, is shifted to positive and negative values. b) The ratio of integrated intensities of the ERS and LO phonon peaks as a function of E_F. c) The LO phonon frequency ω_{LO} upshifts as frequency renormalizing virtual e-h pairs are blocked. d) The linewidth Γ_{LO}, broadened in the window $|E_F| < \hbar\omega_{LO}/2$ within which the LO phonon can decay into a real e-h excitation. e) The E_F evolution of the asymmetry parameter $-1/q$ of the LO peak. The Fermi level scale was estimated by fitting the width of the broadening window in d) to the LO phonon energy [23].

centered at low Raman frequencies, in which case its tail overlaps with the G-band. As the ERS peak approaches the G-band feature, its relative intensity decreases partly because the overlap of these two features matches the condition for a scattered resonance of the G-band. In our data, we have not observed the ERS feature at frequencies higher than the G-band feature. Considering that the ERS feature only appears on the side of the G-band to which the latter known to be skewed, one can imagine how the ERS contribution to the spectrum could be mistaken as part of the tail of the asymmetric LO phonon peak. It is, indeed, easy to overlook the ERS spectrum when the substrate signal is not subtracted, especially when using a higher resolution spectrometer which does not acquire the entire energy range of the Raman spectrum at once. The Fano factor, q, is then quite sensitive to the selected baseline during the curve fitting process. Since our signal is free from a substrate contribution, we fit the spectrum in Fig. 4-1c, without a baseline, using Lorentzian curves for the ERS feature, the RBM and the G^+ feature, and using only a BWF lineshape to fit the G^- feature. With the ERS contribution subtracted, the isolated phonon contribution to the BWF is fit to $I_{LO}(\omega) - I_o$. We approximate I_o as a constant because the ERS is slowly varying with respect to the G-band feature. Even when accounting for the ERS spectrum, the LO phonon peak still exhibits a mildly asymmetric BWF lineshape with $1/q = 0.10$, confirming that the observed asymmetry is not an artifact of the overlap with the ERS feature.

Our study offers a unique opportunity to investigate the coupling between the electronic and phonon Raman processes in carbon nanotubes. The asymmetry of the LO peak is often attributed to an interference between phonon and electronic scattering processes. Here q is a measure of the relative strengths of the interfering pathways and is given by:

$$\frac{1}{q} = V_{ep}\frac{M_e}{M_p}$$

where M_p and M_e are, respectively, the phonon Raman and ERS matrix elements, and V_{ep} is the coupling between the LO phonon and e-h pairs [58]. The coupling is related to the electron-phonon contribution to the phonon linewidth Γ_{e-p}, by the

proportionality $V_{ep} \propto \Gamma_{e-p}^2$. The total phonon linewidth Γ_{LO} includes an intrinsic term which is taken here to be $\sim$ 10 cm^{-1}. Since both the position of the ERS peak and the resonance condition of the LO phonon depend on E_L, we expect that the ratio M_p/M_e in the vicinity of the G-band will also change with E_L. In Fig. 4-5, we take a close look at the LO lineshape by fitting the G-band peaks for each spectrum of Fig. 4-2 a) after having subtracted the ERS background. We find that $1/q$ varies very little when E_L is tuned from 2.0 eV to 2.2eV, but that it decreases strongly for $E_L = 2.33eV$ when the G-band and ERS are almost overlapping. In this case, the G-band is close to being in a scattered resonance with the M_{22}^+ transition and the ERS is weak as noted earlier. Both of these effects contribute in an increase in M_p/M_e and a corresponding decrease in $1/q$. Note that Γ_{LO}, and therefore the electron-phonon coupling term V_{ep}, does not change with E_L. On the other hand, V_{ep} depends strongly on the Fermi energy.

Applying a gate voltage, as in Fig. 4-4, enables us to tune q in a different manner. Blocking the available e-h excitations reduces both M_e and V_{ep} while keeping M_p relatively constant. The changes in $M_e/M_p(E_\mathrm{F})$, $V_{ep}(E_\mathrm{F})$ are reflected in the $I_{ERS}/I_{LO}(E_\mathrm{F})$ and $\Gamma_{LO}(E_\mathrm{F})$ and $q(E_\mathrm{F})$ shown in Figs. 4-4 b), d) and c), respectively. Overall, the changes in $1/q$ brought about by tuning E_L and E_F are qualitatively consistent with the picture of a Fano resonance between the LO phonon and interband e-h pairs. While the ERS can, for certain excitation conditions, be quite strong, the phonon Raman transition is always much stronger in the relevant energy range in which they overlap, thus making the ratio M_e/M_p, and consequently $1/q$, a small number. The large ratio of the phonon to electron Raman intensity explains why the asymmetry is always very weak despite a very strong coupling, V_{ep}, between e-h pairs and the LO phonon due to the Kohn anomaly [31]. The weak Fano interference that we observe in the Raman spectrum of $M-$SWNTs contrasts the much stronger interference observed between optical phonons and excitons in the IR absorption of bilayer graphene [59, 60]. In the latter case, much larger values of $1/q$ are observed since the continuum channel, defined by optical absorption of infrared photons across the bandgap, is much stronger than the contribution to the IR absorption from the

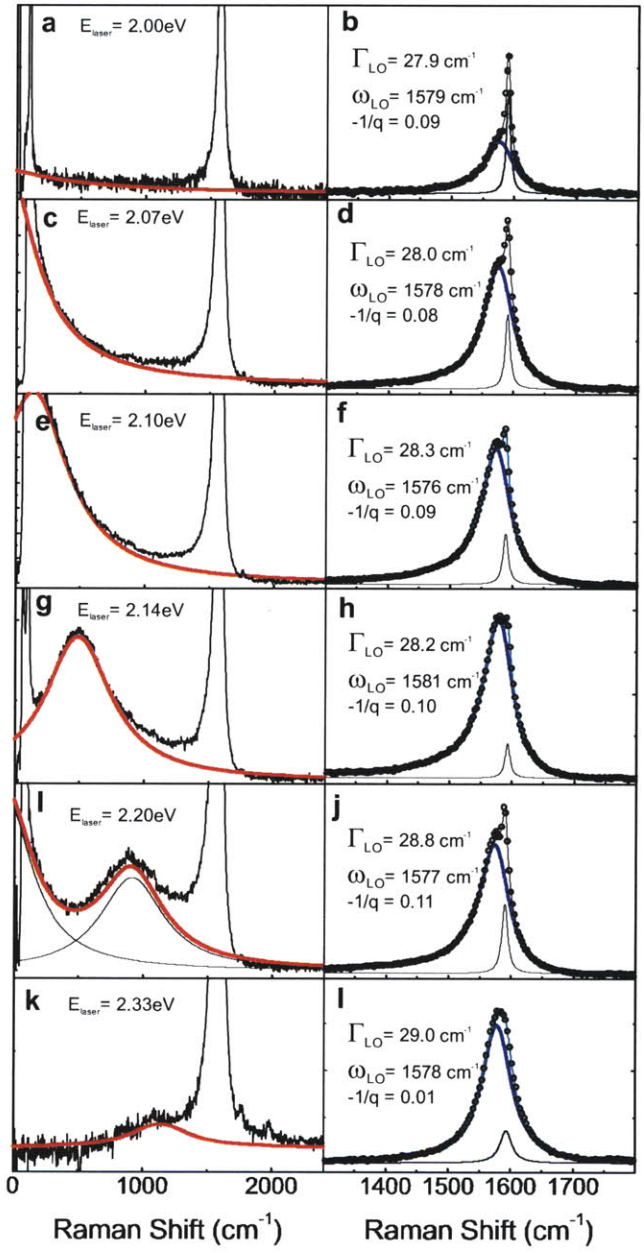

Figure 4-5: The G-band lineshape as a function of laser energy. The left panels show the Lorentzian fits to the ERS background for each indicated E_{L} value for the $M-$SWNT shown in Fig. 4-2 a). The right panels show the fitted G-band spectra after subtracting the ERS background. The values of the linewidth Γ_{LO}, frequency ω_{LO} and asymmetry parameter $-1/q$ are indicated for the LO G-band mode.

optical phonon mode.

4.7 ERS as a characterization tool

Finally, we comment on the utility of the ERS feature for extracting physical information from $M-$SWNTs. A quick method for identifying the M_{ii} energies of $M-$SWNTs is a desirable capability for researchers. Rayleigh scattering provides a quick, one-shot method for finding the optical resonances of any SWNT. However it requires special instrumentation and substrates [47, 61]. Raman spectrometry is a widespread characterization tool in the SWNT field, but can only be used to determine the exact M_{ii} energies if a Raman resonance window is collected [62]. This tedious technique requires a tunable laser, offers poor spectral resolution and is complicated by the overlap of the incoming and outgoing resonances of the phonon modes. ERS, on the other hand, like Rayleigh scattering, is a one-shot measurement and provides good spectral resolution. Moreover, it can be used on an arbitrary substrate and can be measured with any Raman spectrometer. For example, the $M-$SWNT in Fig. 4-2 c) was assigned as a (15,6) nanotube based its ERS peak energies and its RBM frequency. The major limitation of ERS is that it is restricted to nanotubes that are excited near resonance. For an $M-$SWNT whose M_{ii} is within 200 meV below E_{L}, ERS features will appear at the M_{ii} energies in the Raman spectrum, provided that the SWNT is not highly doped. Using a broadband spectrometer, and in the case of SWNTs located on a substrate, subtracting the substrate signal, will facilitate the observation of this feature. Besides providing information about the energy and lifetime of the M_{ii} transition from the position and linewidth of the ERS feature, the ERS spectrum may also contain information about the continuum of the electronic excitations by which the light is scattered. By using a sharper laser cut-off, the lower energy of the ERS could potentially be used to study the structure of the metallic electronic bands at very low energies where $M-$SWNTs are known to exhibit minigaps due to curvature and electron correlation effects [43]. Within our current understanding, we do not expect contribution to the ERS spectrum for energies within the insulating

gap.

4.8 Summary

We have reported the electronic Raman spectrum (ERS), a new feature in the Raman spectrum of metallic carbon nanotubes that arises from a resonantly enhanced scattering by interband electronic excitations. We have shown how the ERS spectrum can be used to identify the exact M_{ii} energies when a M-SWNT is excited near resonance. We have also proposed that the ERS spectrum can be used to the study the low energy electronic structure and electron correlations in M-SWNTs. While phonon Raman scattering has been studied in great detail during the last decade, the topic of ERS has not yet been addressed in detail theoretically. Hopefully the experiments reported here will inspire theoretical work, providing further insight into the nature of the Coulomb interaction in metallic carbon nanotubes.

Chapter 5

Doping dependence of the G' peak: metallicity dependent electromechanical coupling

In chapter 3 we described how the frequencies of certain Raman modes change when the nanotube is charged by the addition of electrons or holes. We showed that charging a metallic nanotube can alter its phonon frequency by reducing the strength of the electron-phonon interaction. In this chapter, we will again study the changes in phonon frequencies while changing the Fermi level. However, by focusing on modes that are not strongly coupled to electronic excitations, we try to extract information on static changes that occur to the lattice when charged. Changes in the C-C bond lengths give rise to modified force constants, and as a result, the lattice vibration (phonon) frequencies are changed. Specifically, we look at the difference in the way metallic and semiconducting nanotubes accommodate extra charge on the lattice.

5.1 Background

5.1.1 SWNT electrochemical actuators

Because of their exceptional mechanical and electrical properties, a promising application of SWNTs is in the area of electromechanical actuators. Nanotube sheet actuators have been shown to operate at low voltages and provide higher work densities than other alternative technologies [63, 64]. Despite these promising results, it is not clear whether the actuation mechanism involves expansion of C-C bonds or repulsion between individual nanotubes in a bundle. Furthermore, it is unclear whether or not the actuation properties of all SWNTs are similar. Experiments at the individual nanotube level are needed but it is very challenging to perform electromechanical measurements on single nanotubes. Raman spectroscopy is capable of detecting small changes in bond length through corresponding changes in the phonon frequencies of C-C stretching modes. We have also demonstrated, in chapter 3, that we are capable of measuring changes in the spectrum of individual SWNT as a function injected charge. Therefore in situ Raman spectroscopy during electrochemical charging is a suitable technique for studying the electromechanical properties of individual SWNTs.

5.1.2 The G' Raman peak

As mentioned above, we would like to avoid Raman peaks whose frequencies are strongly affected by coupling to electronic excitations. In chapter 3 we show that the G-band phonons of metallic nanotubes are strongly coupled to e-h pairs. Semiconducting nanotubes also experience a significant gate dependent frequency shift of the G-band due to e-p coupling [65]. Strong coupling occurs for Γ point and K-point phonons therefore a phonon that does not originate from one of the points is desirable.

The double resonant G' peak involves iTO phonons with wavevectors from close to, but not exactly at, the K-point [9]. Our results show that phonons with wavevectors sufficiently far from this point are not affected by the predicted K-point Kohn

anomaly of metallic nanotubes. Since the phonon in question has a finite wavevector ($q \neq 0$), the conservation of momentum must either be satisfied by an elastic scattering event (giving rise to the D-band) or by scattering with another iTO phonon of equal and opposite q (giving rise to the G'-band). The selected wavevector q that satisfies the double resonance condition is intimately tied to the electronic structure of the nanotube and to the laser excitation energy used.

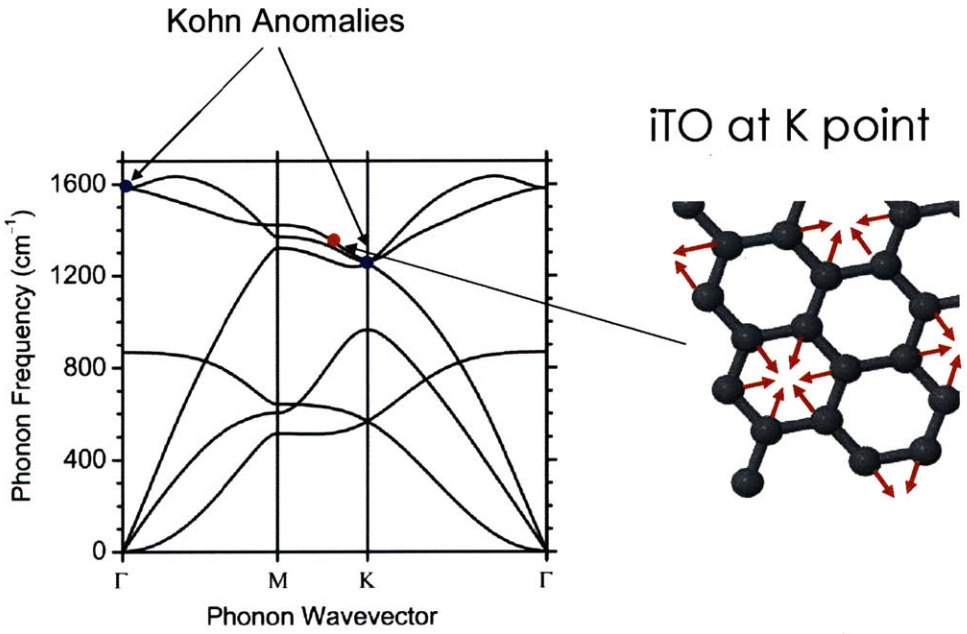

Figure 5-1: a) The phonon dispersion of graphene showing the location of the Γ and K-point Kohn anomalies and showing the segment of the iTO branch from which the G' peak originates b) The deformation of the iTO branch at the K-point showing pertinent displacement vectors with A_1 symmetry.

5.1.3 Deformation induced frequency shift of the G' peak

Since we intend to use the G' frequency $\omega_{G'}$ to detect changes in the bond length, we first discuss the expected shift in $\omega_{G'}$ associated with a given deformation. Expanding

a bond will weaken the force constant and lead to a downshift in frequency, and the opposite is true for the contraction of a bond. A general deformation of a CNT is typically described in terms of its axial and radial components, $\epsilon_{\|}$ and $\epsilon_{\perp}$ or in terms of its isotropic and anisotropic strain components $\epsilon_{iso} = (\epsilon_{\|}+\epsilon_{\perp})/2$ and $\epsilon_{ani} = (\epsilon_{\|}-\epsilon_{\perp})/2$, respectively. The degree to which the frequency of each mode is shifted depends on the deformation pattern on the phonon. The G' phonon originates from the iTO phonon branch near the K-point [9]. Right at the K-point, the iTO branch, having A_1 symmetry, resembles the breathing of the carbon ring, as shown in Fig. 5-1 and thus only the isotropic component of the strain ϵ_{iso} contributes to the shift in phonon frequency. We expect a similar strain dependence for the G' phonon based on recent studies on the strain dependence of the G' peak in graphene [66]. The frequency change as a function of the isotropic strain is given by [66]:

$$\frac{\Delta\omega_{G'}}{\omega_{G'}} = -2\gamma^{q}_{iTO}\epsilon_{iso} \tag{5.1}$$

The Grüneisen parameter, γ^{q}_{iTO}, is a slowly varying function of the wavenumber q, and for the region of the Brillouin zone selected by the double resonance process in our experiments, its value ranges from ~2.5-3 [66]. We assume that, for small strains, any shearing of the hexagonal lattice caused by the anisotropic part of the strain, ϵ_{ani}, does not shift or split the iTO phonon as it does to the doubly degenerate E_{2g} phonons at the Γ point [66]. Based on this mechanism, we expect a frequency shift of $\sim -140 - 160\text{cm}^{-1}/\%\epsilon_{iso}$.

5.1.4 Doping induced deformation

Here we review some of the theory describing charge-induced strain in SWNTs [67, 68, 69, 70]. In-plane dimensional changes due to doping have been studied extensively in graphite intercalation compounds [71]. Negative and positive charge injection cause expansion and contraction of the C-C bond length, respectively. The charge strain behavior is explained in terms of the breaking of e-h symmetry from second-neighbor antibonding interactions [71, 72]. Since the demonstration of CNT electrochemical

actuators [63] the topic of charge-induced deformation of CNTs has been addressed theoretically by a number of methods, with some conflicting results.

Two types of contributions to the charge-induced deformation of SWNTs must be taken into account: 1) the quantum mechanical changes in bond length due to changes in bond ordering when nanotubes are charged 2) expansion of bonds due to the electrostatic (Coulomb) repulsion between atoms when charged. In graphene, the bond ordering contribution dominates and gives rise to a charge-asymmetric deformation [72]. In nanotubes the bond ordering contribution affects ϵ_{iso} and ϵ_{ani} differently. In both M- and S- SWNTs, bond ordering causes an isotropic expansion and contraction of the lattice for hole and electron doping [67, 68], just like in graphene [71, 72]. However, for S-SWNTs bond ordering causes a response in ϵ_{ani} that is symmetric with respect to the sign of charge [67, 68, 69, 70]. Whether this change in ϵ_{ani} is positive or negative depends on the mod($2n + m$,3) type of the S-SWNTs. As mentioned above, we do not expect $\omega_{G'}$ to strongly reflect these anisotropic deformations because of its near-A symmetry [66].

The Coulomb repulsion contribution to the deformation is only predicted to affect ϵ_{iso} and is always charge symmetric [68, 73] . Pastewka et al. [68] show that the relative contributions of the bond ordering and electrostatic contributions to the deformation depend on the dielectric of the surrounding medium.

5.2 Different charge-induced deformations for M-SWNTs and S-SWNTs

The experiments were carried out in the same manner as described in chapter 1. We have here collected spectra from several semiconducting Fig. 5-3 and metallic nanotubes Fig. 5-2 in order to differentiate between their respective behaviors. Most of the nanotubes that we use in this study have an RBM which is used to identify their mod($2n + m$,3) type.

In Fig 5-2 a) we show intensity plots of the G, and G' peaks of an M-SWNT as

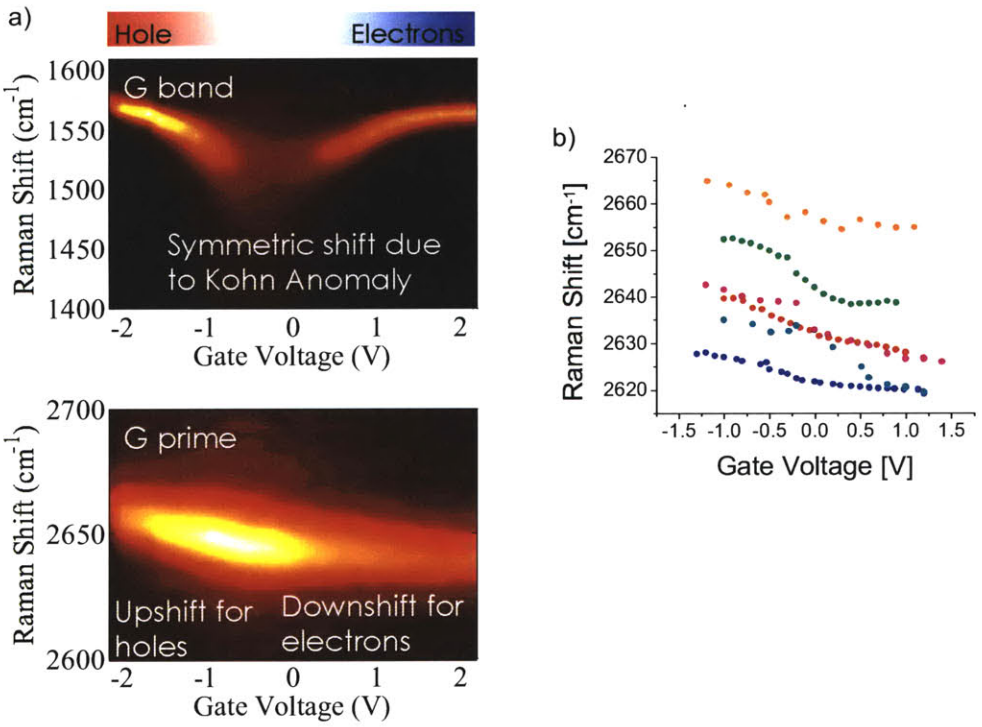

Figure 5-2: a) Intensity plot of the G-band $\omega_G(V_G)$(top) and G' band ($\omega_{G'}(V_G)$ bottom) of an M-SWNT as a function of V_G. b) the G' frequency function of V_G plotted as $\omega_{G'}(V_G)$ for several M-SWNTs.

a function of gate voltage. As in chapter 3, the G-band exhibits a symmetric upshift in frequency about the gate voltage, characteristic of the Kohn anomaly [17]. The G' peak on the other hand upshifts at negative gate potentials and and downshifts for positive potentials. This behavior is qualitatively similar to the response of the G' peak of graphene [57].

The S-SWNTs that we have observed exhibit a variety of behaviors, all different from that of M-SWNTs. The most common behavior is a downshift of the G' frequency for both polarities of gating, as shown in Fig. 5-3 a). The much less common behaviors are: 1) a symmetric upshift of $\omega_{G'}$ about gate voltage V_o (Fig 5-3 b) and 2) no appreciable shift at all (Fig 5-3 c).

To gain insight in the origin of the behaviors of charge-induced frequency shifts,

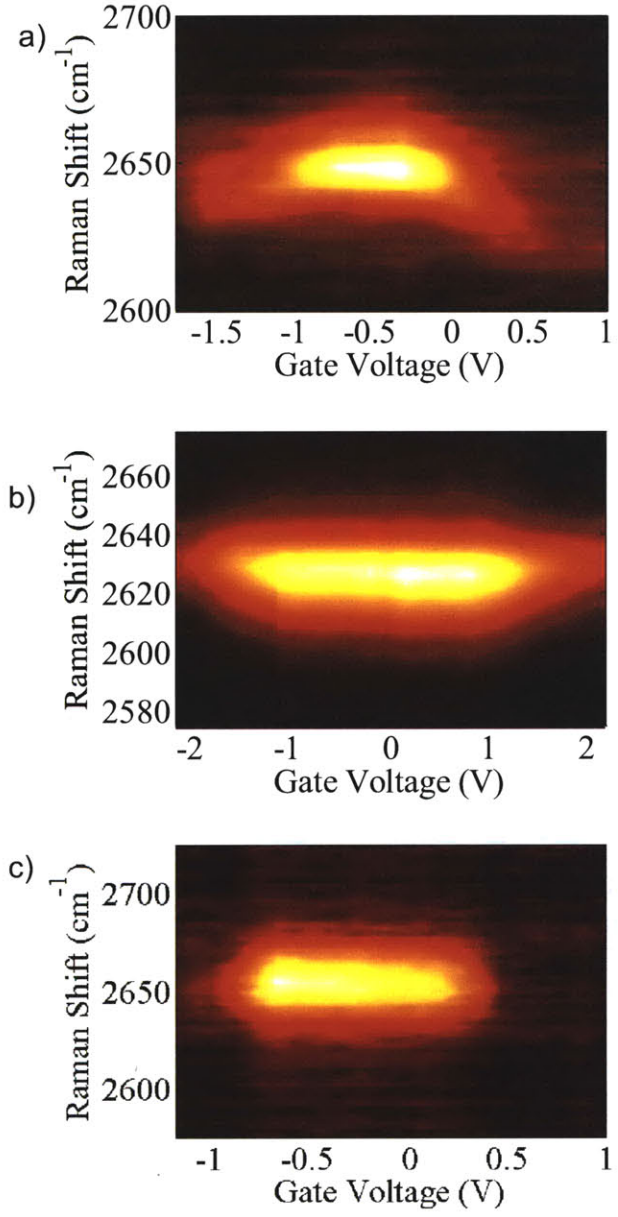

Figure 5-3: Three different behaviors of the $\omega_{G'}(V_G)$ for S-SWNTs. a) downshift for electron/hole doping (most common) b) upshift for electron/hole (rare) doping c) no shift (rare).

we have overlaid these findings onto a theoretical Kataura plot (Fig. 5-4), for those nanotubes under study for which we have observed an RBM peak. As expected, the nanotubes whose change in $\omega_{G'}$ is **odd** with respect to charge polarity (labeled O) line up with the metallic areas of the Kataura plot, while those which **downshift** (D) and **upshift** (U) have been entirely assigned to semiconducting nanotubes in Fig. 5-4. Neither the common downshifting behavior, nor the less abundant upshifting behavior appear to correlate with a particular mod($2n + m$,3) type of S-SWNT.

5.3 Discussion

In M-SWNTs we always observe an upshift of $\omega_{G'}$ for hole doping and a downshift for electron doping. This is the case for nanotubes observed at both the upper and lower metallic transitions M_{ii}^{+} and M_{ii}^{-} and over a large range of diameters and chiral angles. Like in graphene, there is no signature of the K-point Kohn anomaly in $\Delta\omega_{G'}(V_G)$ which would manifest itself as a symmetric upshift with respect to V_G. Rather, we believe the origin of $\Delta\omega_{G'}$ is the expansion and contraction of bonds for electron and hole doping. This behavior is in qualitative agreement with the bond ordering contribution to the isotropic charge-induced deformation described the theory of [67, 68].

In the case of S-SWNTs, we find that $\Delta\omega_{G'}(V_G)$ is always charge symmetric, even though the bond ordering contribution to the isotropic response is expected to be asymmetric like M-SWNTs. A strong charge-symmetric deformation has been predicted in the anisotropic deformation response [67, 68], $\epsilon_{ani}(q)$ of S-SWNTs, but we do not expect this factor to affect $\Delta\omega_{G'}(V_G)$, because the G' mode near the K-point is almost a fully symmetric mode. Furthermore, the predicted sign of the $\epsilon_{ani}(q)$ is different for the two types of S-SWNTs. Nevertheless, we have not found any correlation between the upshifting and downshifting of the $\omega_{G'}$ of S-SWNTs and their mod($2n+m$,3) types. Since the downshifting behavior is the most common behavior for S-SWNTs, it appears as though there is a dominating mechanism causing an expansion of the bonds in most S-SWNTs upon charging. Coulomb repulsion is

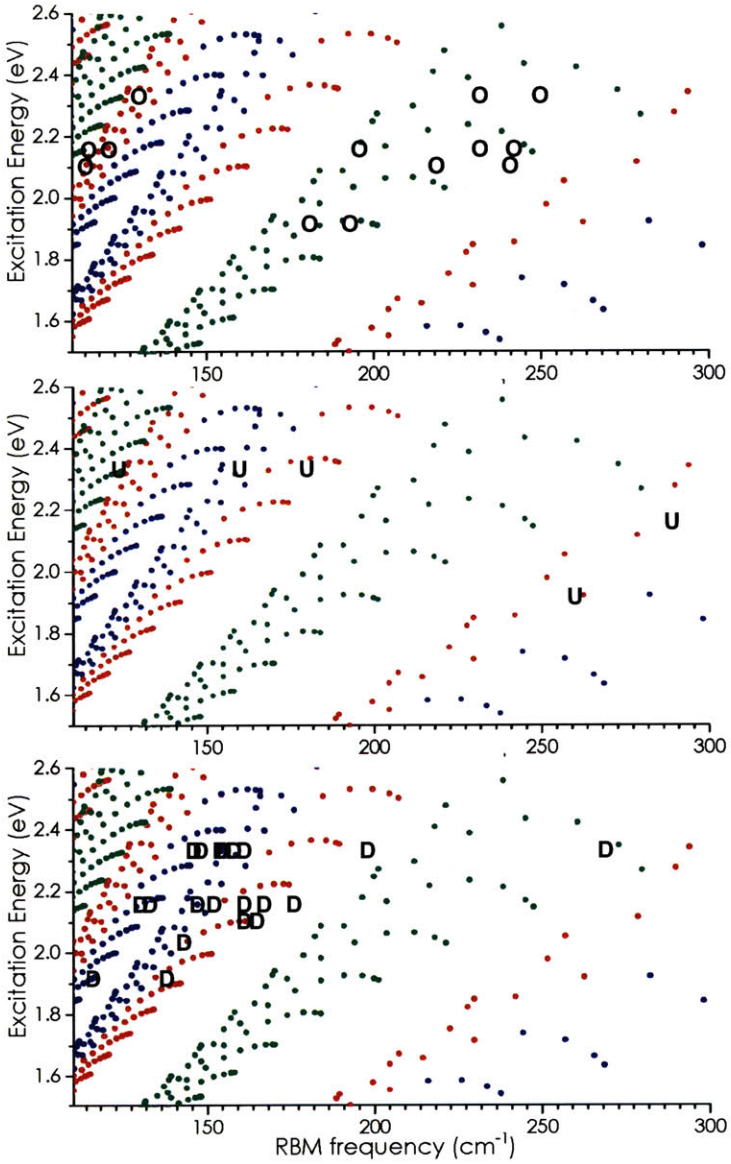

Figure 5-4: Mapping of the different behaviors onto the Kataura plot of E_{laser} vs. ω_{RBM}. O indicates the charge asymmetric $\omega_{G'}$ frequency shift. D and U indicate the charge symmetric downshift and upshift of $\omega_{G'}$. Markers are placed based on the measured RBM frequency of the SWNT and the energy at which it was resonantly excited

expected to causes an isotropic expansion of bonds that is quadratic in charge, and therefore meets the description. However, as noted above, the Coulomb term does not appear to dominate the response of M-SWNTs because there is already charge on the bonds. Pastewka et al. [68] explain that the contribution from the Coulomb repulsion depends on the dielectric constant of the medium. While the dielectric environment surrounding a SWNTs is known to be very important in the context of Coulomb interactions, we know that the charge carriers in the SWNTs themselves also participate in screening [4]. This is demonstrated by the fact that the exciton binding energies of S-SWNTs are an order of magnitude greater in than in M-SWNTs [3, 4]. Based on this argument, it is reasonable to say that electrostatic repulsion due to charging is more important for the G' band spectra of S-SWNTs than it is for M-SWNTs.

5.4 Recent advances on the doping dependence of the G' peak

The doping dependence of the G' peak has previously mostly been investigated in bundles, using a variety of doping methods. Maciel et al. [74, 75] studied bundles of SWNTs that have been substitutionally doped with n-type (phosphorus and nitrogen) and p-type (boron) dopants. They report that this type of doping causes a splitting of the G'-band into two peaks. One component is shown to originate from the defective dopant sites and the other from the pristine segments of the nanotube [74]. The peak associated with the dopant sites are found to upshift for p-type dopants and downshift for n-type dopants. No distinction is made between contributions from metallic and semiconducting nanotubes in this study. In our results, and in other electrochemical gating experiments this splitting of the G' peak is not observed, since the doping due to charge transfer is less localized.

Recently there have have two studies that address on the G' peak of the electrochemically doped SWNT bundles, where the laser energy is picked to resonantly

excite a majority of either semiconducting or metallic SWNTs. Das et al. [76] focus on resonantly excited semiconducting nanotubes and find that the $\omega_{G'}$ downshifts for electron doping and does not shift at all for hole doping. On the electron doping side, this result is consistent with our measurements. The lack of shift observed for the hole doping could be understood if we consider that metallic nanotubes may also be contributing the G' spectrum, in which case the G' peak of the metallic and semiconducting nanotubes would be shifting in opposite directions. This would result in a broadening of the G' peak, which is indeed reported [76].

In another study, Rafailov et. al [77] selectively excite metallic nanotubes within bundles and focus of the frequency of the G' band. They show that there is a symmetric component in the frequency shift with respect to the polarity of the charge, which is evidence for the K-point Kohn Anomaly [31]. Interestingly this effect is only observed at lower excitation energies. These are lower energies than we have used in experiments presented in this chapter. It is possible that the signature of the Kohn Anomaly could be observed in our individual SWNT experiments if we were to probe metallic nanotubes at lower laser energies.

While the last two studies have attempted to resonantly selected certain types of SWNTs within bundles, Kalbac et al. were the first to report the charging dependent G' spectrum of several individual SWNTs. The authors found a variety of behaviors that, like in our study, are not evident from experiments performed on bundles. A sufficient amount of data was not collected to correlate these behaviors with the type of SWNT. Nonetheless, these behaviors reported in [38] are consistent with the data presented in this chapter.

5.5 Summary

We have performed a detailed study of the doping dependence of the double resonance G' peak of individual nanotubes. The G' frequency $\omega_{G'}(V_G)$ of M-SWNTs upshifts with hole doping and downshifts with electron doping. Most S-SWNTs downshift for both signs of doping, but a smaller fraction of them either upshift or do not shift at

all upon doping. We attribute these shifts to charge-induced strain and we reason that in metallic nanotubes the bond ordering contribution to the ϵ_{iso} dominates the charge-induced deformation response while in S-SWNTs the Coulomb repulsion term dominates because of weaker dielectric screening. This result implies that separating of nanotubes based on metallicity and type can improve the effectiveness of nanotube actuators. As discussed above, we believe that the $\omega_{G'}$ is more sensitive to isotropic strain. However the anisotropic strains predicted in the literature [67, 68, 69, 70] are significant and will certainly contribute to the actuation of SWNT mats. Anisotropic strains could be detected independently by measuring the shift in the bandgap as a function of doping.

Chapter 6

Phonon populations during high-bias transport

In this chapter we have monitored the Raman spectra of an electrically contacted SWNTs as a function applied bias across the device. The objective of these combined measurements was to extract information about the temperature of the lattice and populations of the phonons during high-field transport. The work presented here is incomplete, however we present insightful preliminary results that point to future experiments in this area. Since there have been significant recent efforts to combine Raman spectroscopy and electrical transport measurement on carbon nanotube devices, we provide a summary of the most recent findings on this topic at the end of this chapter.

6.1 Background

6.1.1 High-field transport in metallic carbon nanotubes

Metallic carbon nanotubes are excellent electrical conductors but they are limited in how much current they can carry. Each M-SWNT can carry a maximum current of $\sim 25\mu A$ [78]. This saturation of the current at high-fields has been attributed to the onset of optical phonon emission [78]. Theoretical modeling of the current-voltage

(IV) characteristics of a nanotube requires a knowledge of the phonon scattering rates, which depend on both the phonon population and lattice temperature. Lazerri et al. [79] reported that the experimental IV curves could not be reproduced without assuming the optical phonons population to be far out of thermal equilibrium. Later, Pop et al. [80] measured the IV curves of M-SWNTs, suspended in air, and found that their devices exhibited a negative differential conductance. This behavior was attributed to a combination of lattice heating and a non-equilibrium phonon population. The difficulty in modeling the IV characteristics of SWNTS is that many assumptions need to be made about the population of the phonons, the lattice temperature and the thermal coupling to the substrate. The resistance obtained from the IV curve is a value that is integrated over many scattering events; therefore, much of the information about the quantum state of the phonons is lost. For this reason, it is desirable to obtain additional experimental information about the state of the phonons during device operation. In this chapter, we monitor the Raman spectrum of electrically biased SWNTs in order to gain more information about the nanotube temperature and about the population of individual phonon modes. We have fabricated devices made of isolated carbon nanotubes that are electrically contacted by source and drain electrodes. We have simultaneously applied a current across nanotube devices and collected the Stokes and anti-Stokes Raman spectra from which we were able to determine the individual phonon temperatures.

6.1.2 Stokes/antiStokes Raman spectroscopy

The ratio of the Stokes to antiStokes (S/AS) Raman intensity is given by:

$$\frac{I_S}{I_{AS}} = A \exp\left(\frac{E_{ph}}{k_B T}\right) \tag{6.1}$$

where

$$A = \frac{E_L - E_{ii} - \hbar\omega_{ph} + i\Gamma}{E_L - E_{ii} + \hbar\omega_{ph} + i\Gamma}. \tag{6.2}$$

Here, E_L is the laser energy, and E_{ii} and Γ_{ii} are the transition energy and width, respectively. If we assume that E_{ii} is not changing as a function of voltage, and that the nanotube is at room temperature at zero bias, then only the change in I_S/I_{AS} is needed to estimate the phonon population. The temperature of the phonon is then given by:

$$T_{ph}(V_B) = \left[\frac{1}{T_o} - \frac{k_B}{E_{ph}} \ln \frac{\left(\frac{I_S}{I_{AS}}\right)_{V=V_B}}{\left(\frac{I_S}{I_{AS}}\right)_{V=0}} \right]^{-1} . \tag{6.3}$$

6.2 Device fabrication

Long aligned nanotubes were grown as in [22] on a Si substrate with a 100nm of dry thermal SiO_2 grown on top. We performed a linear spatial Raman map of the substrate that collected a spectrum every 500nm over a distance of 1 cm to find metallic nanotubes of interest. The locations of these nanotubes were marked with respect to macroscopic cross hairs on the edge of the chip. A layer of S1813 positive photoresist was spin coated onto the sample which was then soft baked. The chip was returned to the Raman microscope where the motorized stage was used to return to the position of each of the metallic nanotubes of interest. The motorized stage was automated to write a pattern of alignment marks into the photoresist using the 532nm laser focused onto the sample. The sample was then taken to an optical photolithography mask aligner where an electrode pattern was stepped to each set of alignment marks and the photoresist was exposed. After development, 5nm of Cr and 30nm of Au was evaporated on to the pattern and the remaining metal was lifted off using acetone. Figure 6-1 is a scanning electron micrograph of a nanotube device.

6.3 Combined Raman and transport measurements

In a first set of experiments we study the Stokes and antiStokes spectra of a M-SWNT device as a function of applied bias, but at a fixed laser energy. Next, we present experiments where we have swept the laser energy in order to determine the resonance

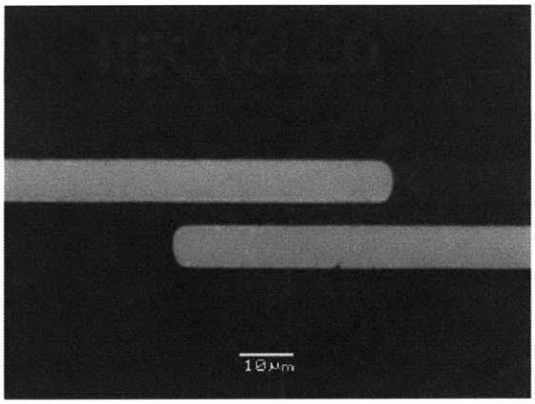

Figure 6-1: A scanning electron micrograph of the a M-SWNT contacted by source and drain electrodes

Raman profile (RRP) of the phonon modes as a function of applied bias.

6.3.1 Bias induced changes in LO/TO temperatures

In Figure 6-3, we show the zero bias Stokes G-band spectrum of a M-SWNT device, which we have fit to two peaks. As in chapter 3, we have assigned the G^+ and G^- peaks of the nanotube to the LO and TO modes, respectively. We have collected both the Stokes and the antiStokes spectra as a function of applied drain-source bias, while also measuring the current which is shown in Fig. 6-2 a). As expected, the current begins to level off near 25 μA. Figure 6-2 b) and c) are intensity plots of the Stokes and antiStokes G-band spectra showing a decrease in the Stokes intensity and an increase in the antiStokes intensity with increasing bias. We fit the LO and TO peaks at each bias level, and show the phonon temperatures derived from the S/AS ratio in Fig. 6-4. From 0 to 8V the LO and TO temperatures appear to increase by a modest 180K and 125K, respectively.

In Figure 6-5, we show the change in frequency and linewidth of the LO and TO peaks. The temperature-dependent frequency of a phonon depends on the temperature of the phonons into which it decays, while the linewidth is a measure of its decay rate [81]. The TO mode shows a very small decrease in frequency and increase in linewidth. On the other hand, the LO mode exhibits a noticeable upshift in fre-

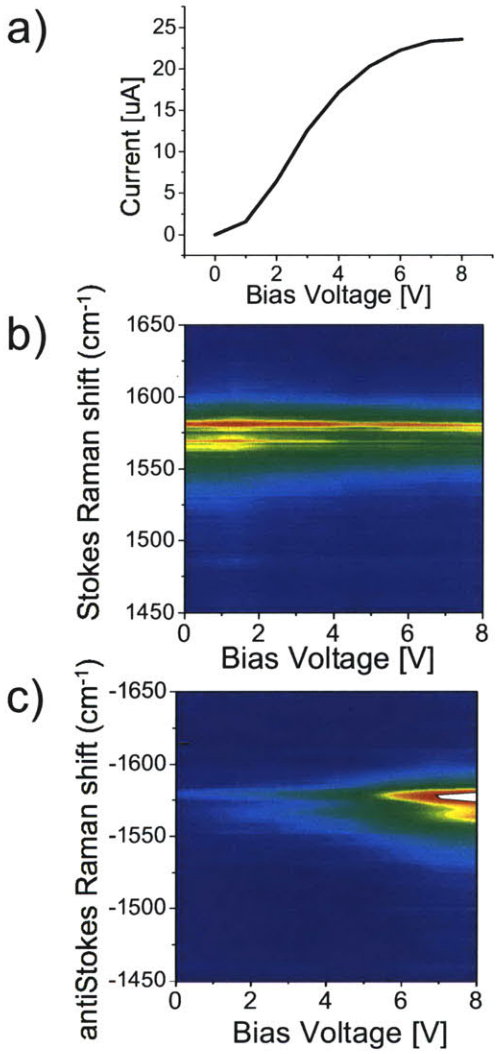

Figure 6-2: a) IV curve collected during simultaneous transport and Raman experiment. Intensity plot of the Stokes a) and antiStokes b)G-band spectra as a function of bias

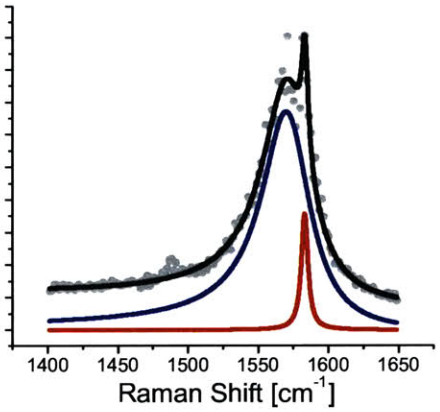

Figure 6-3: The Stokes G-band spectrum of a M-SWNT fitted to two peaks.

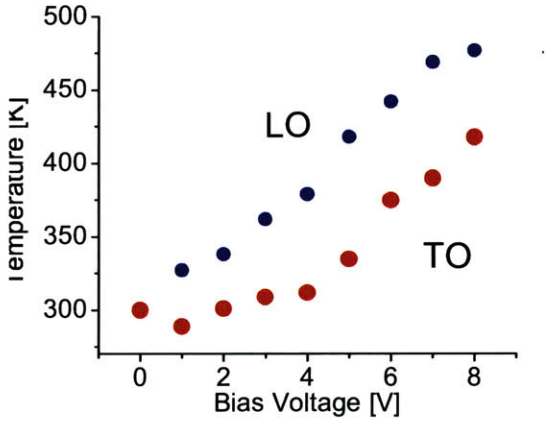

Figure 6-4: The computed phonon temperatures for the LO (blue) and TO (red) modes using the Stokes/anti-Stokes ratio for the same M-SWNT a Fig. 6-3.

quency and narrowing of the linewidth. This anomalous behavior of the LO mode upon heating is likely related to a decoupling of the phonon to electron-hole pairs, (see chapter 3), when the electron temperature is raised.

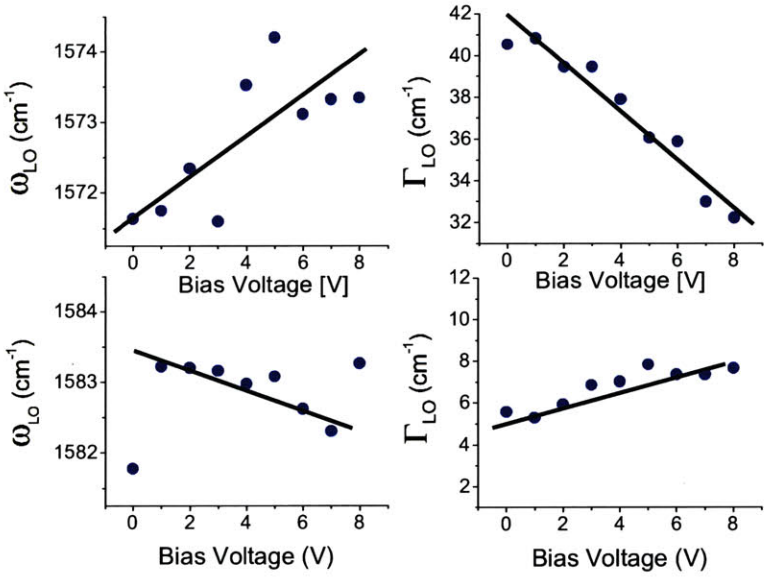

Figure 6-5: The LO and TO frequencies and linewidths as a function of bias voltage for the same M-SWNT as Fig. 6-3.

6.3.2 Bias-induced changes in the resonance window

The analysis in section 6.3.1 assumes that the resonance condition does not deviate significantly when the nanotube is electrically heated. Here we show that this assumption may not be correct. In Fig. 6-6 we show the RBM resonance profile for a S-SWNT nanotube as a function of bias voltage. As the voltage is increased from the 0 to 8V, there is a redshift of ~ 22 meV in the energy of the resonance window. The shift is accompanied by a broadening of ~ 56 meV in the FWHM intensity. This is likely to be caused by the heating of the nanotube. Cronin et al. [82] have studied the temperature dependence of optical transition energies in SWNTs and they find that there is a downshift and a broadening of the resonance profile. The change in the resonance profile as a function of the bias is important because it indicates that the assumption that the resonance term A remains constant throughout the experiment, is incorrect. In order to get the correct phonon temperature for the Stokes/antiStokes ratio, it would be necessary to follow the resonance by measuring the resonance pro-

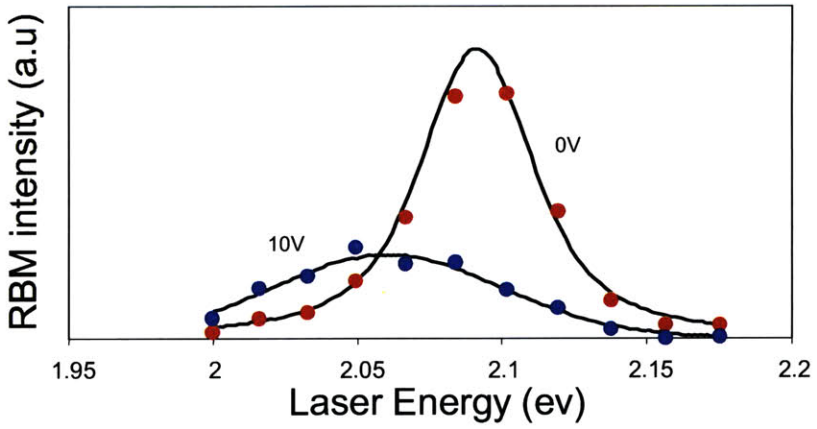

Figure 6-6: Change in the RBM resonance Raman profile of a S-SWNT as a function of bias voltage.

files on the both Stokes and antiStokes sides at each bias voltage.

6.3.3 Recent advances in combined Raman and transport measurements on SWNTs

This above mentioned approach has recently been followed by [83] in a study of phonon temperatures in semiconducting devices. By collecting the Stokes and anti-Stokes resonance windows of both RBM and G-band features, the authors estimate the temperatures of these phonons, while accounting for for the shift in the resonance energy. The data indicates that, in the studied device, the G-band phonons reach a slightly higher temperature than the RBM phonon, which is assumed to be thermalized with the lattice. The authors further estimate the temperatures of the K-point optical phonon and intermediate frequency phonons, based on the spectral widths of the RBM resonance window and the G-band phonon peak, respectively. Both the K-point optical phonon and the intermediate frequency phonons are found to reach a much higher temperature than the G-band and RBM phonons.

Non-equilibrium phonons populations have also been reported in metallic nanotubes. Oron-carl et al. measured the S/AS ratio of the G-band and RBM of several

M-SWNT devices. In a small fraction of devices (3%) the increase the G-band temperature was observed while the RBM temperature remained relatively unchanged, thus suggesting that a non-equlibrium population of G-band optical phonons. In this work the frequency of the G-band does not change with applied bias. In another work, Bushmaker et al. studied the G-band spectrum of suspended M-SWNT devices as a function of applied bias. The SWNTs in the studies described above, have all been on an SiO_2 substrate. Bushmaker et al. observed that the G^+ and G^- features shift in frequency at different rates as a function of bias voltage. In some devices, the G^+ peak is reported to dowhshifts with bias while the G^- does not, and in other cases, the opposite is observed. While the authors suggest that the frequencies of the phonons are an indication of their own temperature, it is more likely that these frequencies reflect the temperature of the phonon baths to which they couple. In either case, this result is an indication of a non-equilibrium phonon population.

6.4 Summary

In this section, we described preliminary results from experiments that are intended to measure phonon populations when large currents are passed through a SWNT. Changes in the S/AS intensity ratio for the G-band phonons indicate that the phonon populations are increasing as a function of bias. However, our study of resonance Raman profile of the RBM as function of applied bias, as well as recent result form the literature, indicate that there is also a change in E_{ii} as a bias is applied, which limits our ability to correctly quantify the population of the G-band phonon. Because of the change in the resonance condition, further experiments are required in order to obtain correct temperature estimates using the S/AS ratio.

Chapter 7

Conclusions

7.1 Summary

While Raman spectroscopy of carbon nanotubes has become a well established area of research during the last decade, many aspects of the Raman spectra of individual nanotubes have yet to be fully explained. This thesis has helped clarify several features of the Raman spectra of metallic carbon nanotubes that have been heavily debated in recent years.

We began by investigating the Fermi level dependence of the G-band spectrum of metallic nanotubes. The changes in linewidth and frequency as a function of occupancy of the valence and conduction bands confirmed that the observed characteristically broadened and downshifted metallic G-band, is due to the coupling of LO phonons to low energy electron-hole pairs. We further demonstrated that virtual e-h pairs may also couple to the radial breathing mode phonon, thereby renormalizing its energy. Next we showed the same e-h excitations which couple to phonons via the e-p interaction may scatter optically excited electron holes pairs via the coulomb interaction, thereby giving rise to an electronic Raman spectrum (ERS). This is the first experimental measurement of the ERS spectrum in carbon nanotubes. While ERS is important on its own, the overlap of the ERS spectrum with the phonon Raman spectrum is very relevant to the interpretation of the G-band spectrum of M-SWNTs. The analysis of the very mild interference between these two scattering mechanism

has helped explain the origin of the asymmetry of the LO peak. In chapter 5, we studied the charge-induced lattice deformations that occur in individual nanotubes by studying the doping dependence of the G' peak. These measurements are important in understanding the microscopic mechanisms involved macroscopic nanotube-based electrochemical actuators. We demonstrated that the actuation properties of metallic nanotubes are similar to graphene while semiconducting nanotubes behave differently. This notable difference between the behavior of metallic and semiconducting nanotubes can also be used to differentiate contributions to the G' peak from metallic and semiconducting nanotubes. Finally we used Raman spectroscopy as a tool to monitor lattice and phonon heating in of metallic carbon nanotube during high field transport.

7.2 Future Work

Experiments on (n, m) identified nanotubes

Many of the observation made in this thesis would not have been possible if the experiments were not performed at the individual nanotube level. The samples used contained both isolated nanotubes and small bundles of SWNTs, but care was taken to use spectra for which the signal appeared to only come from a single nanotube. In some cases, using the RBM frequency and resonant excitation energy, the (n, m) index could be estimated, but in other cases, this could not be done. The uncertainty caused by making an incorrect (n, m) assignment or by mistaking a small bundle for an isolated nanotube has limited the confidence with which we can pinpoint where the theory is lacking. In chapter 4, we used Rayleigh scattering to unambiguously assign three isolated metallic nanotubes. While this is tedious work, many experiments performed in this thesis could have benefited from working with nanotubes of well-defined structures. For example, in chapter 3, we describe work by Sasaki et al. [17] that predicts subtle differences in the Fermi level dependence of the TO mode of metallic nanotubes, which we were not able to observe. In our study of the RBM phonon softening, we were not able to find many of the chiralities to complete the

comparison with theory, because they are difficult to find using Raman. Further, in chapter 5, a clear comparison between the electromechanical coupling occurring in type I and II S-SWNTs was not possible. Therefore we believe that a great deal of insight can be gained by simply repeating many of the experiments performed here on nanotubes that are more clearly isolated and of known (n, m) indices.

Electronic Raman spectroscopy

There are many open issues related to the electronic Raman scattering effect that we observed in chapter 4. Time resolved experiments can be used to truly distinguish the ERS spectrum from radiative recombination, as well as to study the dynamics of the e-h excitations and deexcitations. Moreover ERS can be used to study the spectrum of low energy e-h pairs in metallic nanotubes, thus allowing a fully optical way of studying the band structure near the Dirac point. This is of particular interest in light of recent observations of a Mott insulating state in metallic nanotubes.

Non-equilibrium phonon populations during transport

The combined transport and Raman experiments of chapter 6 have produced preliminary results that are interesting but incomplete. There are a number of discrepancies between publications on this topic . One open question is why the LO and TO modes of metallic nanotubes shift in frequency at different rates, and why they don't shift at all in other publications. Continued effort on this topic using truly isolated nanotubes in devices with high quality contacts, combined by tracking the resonances of the nanotubes with Rayleigh scattering and monitoring the phonon populations via tunable Stokes and antiStokes spectroscopy should make important contributions to this work.

Bibliography

[1] R. Saito, G. Dresselhaus, and M. S. Dresselhaus. *Physical Properties of Carbon Nanotubes*. Imperial College Press, September 1998.

[2] M.S. Dresselhaus, G. Dresselhaus, R. Saito, and A. Jorio. Raman spectroscopy of carbon nanotubes. *Physics Reports*, 409(2):47 – 99, 2005.

[3] J. Maultzsch, H. Telg, S. Reich, and C. Thomsen. Radial breathing mode of single-walled carbon nanotubes: Optical transition energies and chiral-index assignment. *Phys. Rev. B*, 72(20):–, 2005.

[4] F. Wang, D. J. Cho, B. Kessler, J. Deslippe, P. J. Schuck, S. G. Louie, A. Zettl, T. F. Heinz, and Y. R. Shen. Observation of excitons in one-dimensional metallic single-walled carbon nanotubes. *Physical Review Letters*, 99(22):–, 2007.

[5] R. Saito, G. Dresselhaus, and M. S. Dresselhaus. Trigonal warping effect of carbon nanotubes. *Phys. Rev. B*, 61(4):2981–2990, Jan 2000.

[6] Ken ichi Sasaki, Hootan Farhat, Riichiro Saito, and Mildred S. Dresselhaus. Kohn anomaly in raman spectroscopy of single wall carbon nanotubes. *Physica E: Low-dimensional Systems and Nanostructures*, In Press, Corrected Proof:–, 2010.

[7] S. Piscanec, M. Lazzeri, J. Robertson, A.C. Ferrari, and F. Mauri. *Phys. Rev. B*, 75:035427, 2007.

[8] P. T. Araujo, C. Fantini, M. M. Lucchese, M. S. Dresselhaus, and A. Jorio. The effect of environment on the radial breathing mode of supergrowth single wall carbon nanotubes. *Applied Physics Letters*, 95(26):261902–+, December 2009.

[9] R. Saito, A. Gruneis, G. G. Samsonidze, V. W. Brar, G. Dresselhaus, M. S. Dresselhaus, A. Jorio, L. G. Cancado, C. Fantini, M. A. Pimenta, and A. G. Souza. Double resonance raman spectroscopy of single-wall carbon nanotubes. *New Journal of Physics*, 5:–, 2003.

[10] S. D. M. Brown, A. Jorio, P. Corio, M. S. Dresselhaus, G. Dresselhaus, R. Saito, and K. Kneipp. Origin of the breit-wigner-fano lineshape of the tangential g-band feature of metallic carbon nanotubes. *Physical Review B*, 6315(15):–, 2001.

[11] M. Paillet, P. Poncharal, A. Zahab, J. L. Sauvajol, J. C. Meyer, and S. Roth. Vanishing of the breit-wigner-fano component in individual single-wall carbon nanotubes. *Physical Review Letters*, 94(23):–, 2005.

[12] Y. Wu, J. Maultzsch, E. Knoesel, B. Chandra, M. Y. Huang, M. Y. Sfeir, L. E. Brus, J. Hone, and T. F. Heinz. Variable electron-phonon coupling in isolated metallic carbon nanotubes observed by raman scattering. *Phys. Rev. Lett.*, 99(2):027402, 2007.

[13] M. Oron-Carl, F. Hennrich, M. M. Kappes, H. V. Lohneysen, and R. Krupke. On the electron-phonon coupling of individual single-walled carbon nanotubes. *Nano Letters*, 5(9):1761–1767, 2005.

[14] O. Dubay, G. Kresse, and H. Kuzmany. Phonon softening in metallic nanotubes by a peierls-like mechanism. *Phys. Rev. Lett*, 88(23):235506, 2002.

[15] J Kroger. Electron phonon coupling at metal surfaces. *Reports on Progress in Physics*, 69(4):899, 2006.

[16] Nicolas Caudal, A. Marco Saitta, Michele Lazzeri, and Francesco Mauri. Kohn anomalies and non-adiabaticity in doped carbon nanotubes. *Phys. Rev. B*, 75:115423, 2007.

[17] K. Sasaki, R. Saito, G. Dresselhaus, M. S. Dresselhaus, H. Farhat, and J. Kong. Curvature-induced optical phonon frequency shift in metallic carbon nanotubes. *Phys. Rev. B*, 77(24):245441, 2008.

[18] K. Sasaki, R. Saito, G. Dresselhaus, M. S. Dresselhaus, H. Farhat, and J. Kong. Chirality dependent frequency shift of radial breathing mode in metallic carbon nanotubes. *Phys. Rev. B*, 2008.

[19] C. G. Lu, Q. Fu, S. M. Huang, and J. Liu. Polymer electrolyte-gated nanotube field-effect carbon transistor. *Nano Letters*, 4(4):623–627, 2004.

[20] G. P. Siddons, D. Merchin, J. H. Back, J. K. Jeong, and M. Shim. Highly efficient gating and doping of carbon nanotubes with polymer electrolytes. *Nano Letters*, 4(5):927–931, 2004.

[21] A. Reina, M. Hofmann, D. Zhu, and J. Kong. Growth mechanism of long and horizontally aligned carbon nanotubes by chemical vapor deposition. *Journal of Physical Chemistry C*, 111(20):7292–7297, 2007.

[22] M. Hofmann, D. Nezich, A. Reina, and J. Kong. In-situ sample rotation as a tool to understand chemical vapor deposition growth of long aligned carbon nanotubes. *Nano Letters*, 8(12):4122–4127, 2008.

[23] H. Farhat, H. Son, G. G. Samsonidze, S. Reich, M. S. Dresselhaus, and J. Kong. Phonon softening in individual metallic carbon nanotubes due to the kohn anomaly. *Phys. Rev. Lett.*, 99(14):145506, 2007.

[24] C. Thomsen, S. Reich, P. M. Rafailov, and H. Jantoljak. *Physica status solidi*, 214:r15, 1999.

[25] A. Jorio, M. A. Pimenta, A. G. Souza Filho, Ge. G. Samsonidze, A. K. Swan, M. S. Unlu, B. B. Goldberg, R. Saito, G. Dresselhaus, and M. S. Dresselhaus. *Phys. Rev. Lett.*, 90:107403, 2003.

[26] Khoi T Nguyen, Anshu Gaur, and Moonsub Shim. Fano lineshape and phonon softening in single isolated metallic carbon nanotubes. *Phys. Rev. Lett.*, 98:145504, 2007.

[27] Anshu Gaur and Moonsub Shim. Substrate-enhanced $o2$ adsorption and complexity in the raman g -band spectra of individual metallic carbon nanotubes. *Phys. Rev. B*, 78(12):125422, Sep 2008.

[28] Y. Wu, J. Maultzsch, E. Knoesel, B. Chandra, M. Huang, M. Y Sfeir, L. Brus, J. Hone, and T. F Heinz. *Phys. Rev. Lett.*, 99:027402, 2007.

[29] A. W. Bushmaker, V. V. Deshpande, S. Hsieh, M. W. Bockrath, and S. B. Cronin. Direct observation of born-oppenheimer approximation breakdown in carbon nanotubes. *Nano Letters*, 9(2):607–611, 2009.

[30] M Cardona, F Cerdiera, and T.A Fjeldly. Sign of the raman tensor of diamond and zinc-blende-type semiconductors. *Phys. Rev. B*, 10:3433, 1974.

[31] S. Piscanec, M. Lazzeri, J. Robertson, A. C. Ferrari, and F. Mauri. Optical phonons in carbon nanotubes: Kohn anomalies, peierls distortions, and dynamic effects. *Physical Review B*, 75(3):–, 2007.

[32] Khoi T Nguyen, Anshu Gaur, and Moonsub Shim. Fano lineshape and phonon softening in single isolated metallic carbon nanotubes, 2007.

[33] V. Perebeinos, J. Tersoff, and P. Avouris. Electron-phonon interaction and transport in semiconducting carbon nanotubes. *Phys. Rev. Lett.*, 94(8):–, 2005.

[34] H. Farhat, K. Sasaki, M. Kalbac, M. Hofmann, R. Saito, M. S. Dresselhaus, and J. Kong. Softening of the radial breathing mode in metallic carbon nanotubes. *Phys. Rev. Lett.*, 102(12):126804, Mar 2009.

[35] P. T. Araujo, I. O. Maciel, P. B. C. Pesce, M. A. Pimenta, S. K. Doorn, H. Qian, A. Hartschuh, M. Steiner, L. Grigorian, K. Hata, and A. Jorio. Nature of the constant factor in the relation between radial breathing mode frequency and tube diameter for single-wall carbon nanotubes. *Phys. Rev. B*, 77(24):–, 2008.

[36] Jun Yan, Yuanbo Zhang, Philip Kim, and Aron Pinczuk. Electric field effect tuning of electron-phonon coupling in graphene. *Phys. Rev. Lett.*, 98(16):166802, Apr 2007.

[37] J. C. Tsang, M. Freitag, V. Perebeinos, J. Liu, and P. Avouris. Doping and phonon renormalization in carbon nanotubes. *Nature Nanotechnology*, 2(11):725–730, 2007.

[38] M. Kalbac, H. Farhat, L. Kavan, J. Kong, and M. S. Dresselhaus. Competition between the spring force constant and the phonon energy renormalization in electrochemically doped semiconducting single-walled carbon nanotubes. *Nano Letters*, 8(10):3532–3537, 2008.

[39] Stefano Piscanec, Michele Lazzeri, John Robertson, Andrea Carlo Ferrari, and Francesco Mauri. Optical phonons in carbon nanotubes: Kohn anomalies, peierls distortions and dynamic effects. *Phys. Rev. B*, 75:035427, 2006.

[40] M. Y. Huang, Y. Wu, B. Chandra, H. Yan, Y. Shan, T. F. Heinz, and J. Hone. Direct measurement of strain-induced changes in the band structure of carbon nanotubes. *Phys. Rev. Lett.*, 100(13):136803, 2008.

[41] Ge. G. Samsonidze, E. B. Barros, R. Saito, J. Jiang, G. Dresselhaus, and M. S. Dresselhaus. Electron-phonon coupling mechanism in two-dimensional graphite and single-wall carbon nanotubes. *Phys. Rev. B*, 75(15):155420, 2007.

[42] M. Ouyang, J. L. Huang, C. L. Cheung, and C. M. Lieber. Energy gaps in "metallic" single-walled carbon nanotubes. *Science*, 292(5517):702–705, 2001.

[43] Vikram V. Deshpande, Bhupesh Chandra, Robert Caldwell, Dmitry S. Novikov, James Hone, and Marc Bockrath. Mott Insulating State in Ultraclean Carbon Nanotubes. *Science*, 323(5910):106–110, 2009.

[44] A. Pinczuk and G. Abstreiter. *Light Scattering in Solids V*. Springer-Verlag, Berlin, 1989.

[45] Thomas P. Devereaux and Rudi Hackl. Inelastic light scattering from correlated electrons. *Rev. Mod. Phys.*, 79(1):175–233, Jan 2007.

[46] Stéphane Berciaud, Christophe Voisin, Hugen Yan, Bhupesh Chandra, Robert Caldwell, Yuyao Shan, Louis E. Brus, James Hone, and Tony F. Heinz. Excitons and high-order optical transitions in individual carbon nanotubes: A rayleigh scattering spectroscopy study. *Phys. Rev. B*, 81(4):041414, Jan 2010.

[47] M. Y. Sfeir, T. Beetz, F. Wang, L. M. Huang, X. M. H. Huang, M. Y. Huang, J. Hone, S. O'Brien, J. A. Misewich, T. F. Heinz, L. J. Wu, Y. M. Zhu, and L. E. Brus. Optical spectroscopy of individual single-walled carbon nanotubes of defined chiral structure. *Science*, 312(5773):554–556, 2006.

[48] M. S. Dresselhaus, G. Dresselhaus, R. Saito, and A. Jorio. Raman spectroscopy of carbon nanotubes. *Physics Reports*, 409:47–99, March 2005.

[49] H. Son, A. Reina, G. G. Samsonidze, R. Saito, A. Jorio, M. S. Dresselhaus, and J. Kong. Raman characterization of electronic transition energies of metallic single-wall carbon nanotubes. *Physical Review B*, 74(7):–, 2006.

[50] A. Hagen. Electronic structure and dynamics of optically excited single-wall carbon nanotubes. *Applied Physics A*, 751:449, Jan 2002.

[51] V. Perebeinos, J. Tersoff, and P. Avouris. Radiative lifetime of excitons in carbon nanotubes. *Nano Letters*, 5(12):2495–2499, 2005.

[52] Catalin D. Spataru, Sohrab Ismail-Beigi, Rodrigo B. Capaz, and Steven G. Louie. Theory and ab initio calculation of radiative lifetime of excitons in semiconducting carbon nanotubes. *Phys. Rev. Lett.*, 95(24):247402, Dec 2005.

[53] Stéphane Berciaud, Laurent Cognet, and Brahim Lounis. Luminescence decay and the absorption cross section of individual single-walled carbon nanotubes. *Phys. Rev. Lett.*, 101(7):077402, Aug 2008.

[54] C. Manzoni, A. Gambetta, E. Menna, M. Meneghetti, G. Lanzani, and G. Cerullo. Intersubband exciton relaxation dynamics in single-walled carbon nanotubes. *Physical Review Letters*, 94(20):–, 2005.

[55] J. S. Lauret, C. Voisin, G. Cassabois, C. Delalande, P. Roussignol, O. Jost, and L. Capes. Ultrafast carrier dynamics in single-wall carbon nanotubes. *Physical Review Letters*, 90(5):–, 2003.

[56] A. Jorio, G. Dresselhaus, and M. S. Dresselhaus. *Carbon nanotubes : advanced topics in the synthesis, structure, properties and applications*. Springer-Verlag, 2009.

[57] Simone Pisana, Michele Lazzeri, Cinzia Casiraghi, Kostya S. Novoselov, A. K. Geim, Andrea C. Ferrari, and Francesco Mauri. Breakdown of the adiabatic born-oppenheimer approximation in graphene. *Nat Mater*, 6(3):198–201, 2007.

[58] Fernando Cerdeira, T. A. Fjeldly, and M. Cardona. Effect of free carriers on zone-center vibrational modes in heavily doped p-type si. ii. optical modes. *Phys. Rev. B*, 8(10):4734–4745, Nov 1973.

[59] Tsung-Ta Tang, Yuanbo Zhang, Cheol-Hwan Park, Baisong Geng, Caglar Girit, Zhao Hao, Michael C. Martin, Alex Zettl, Michael F. Crommie, Steven G. Louie, Y. Ron Shen, and Feng Wang. A tunable phonon-exciton fano system in bilayer graphene. *NATURE NANOTECHNOLOGY*, 5(1):32–36, JAN 2010.

[60] A. B. Kuzmenko, L. Benfatto, E. Cappelluti, I. Crassee, D. van der Marel, P. Blake, K. S. Novoselov, and A. K. Geim. Gate tunable infrared phonon anomalies in bilayer graphene. *Phys. Rev. Lett.*, 103(11):116804, Sep 2009.

[61] M. Y. Sfeir, F. Wang, L. M. Huang, C. C. Chuang, J. Hone, S. P. O'Brien, T. F. Heinz, and L. E. Brus. Probing electronic transitions in individual carbon nanotubes by rayleigh scattering. *Science*, 306(5701):1540–1543, 2004.

[62] A. Jorio, A. G. Souza Filho, G. Dresselhaus, M. S. Dresselhaus, R. Saito, J. H. Hafner, C. M. Lieber, F. M. Matinaga, M. S. S. Dantas, and M. A. Pimenta. Joint density of electronic states for one isolated single-wall carbon nanotube studied by resonant raman scattering. *Phys. Rev. B*, 63(24):245416, Jun 2001.

[63] R. H. Baughman, C. X. Cui, A. A. Zakhidov, Z. Iqbal, J. N. Barisci, G. M. Spinks, G. G. Wallace, A. Mazzoldi, D. De Rossi, A. G. Rinzler, O. Jaschinski, S. Roth, and M. Kertesz. Carbon nanotube actuators. *Science*, 284(5418):1340–1344, 1999.

[64] G. M. Spinks, G. G. Wallace, C. Carter, D. Zhou, L. S. Fifield, C. Kincaid, and R. H. Baughman. Conducting polymer, carbon nanotube and hybrid actuator materials. *Smart Structures and Materials 2001: Electroactive Polymer Actuators and Devices*, 4329:199–208 524, 2001.

[65] J. C. Tsang, M. Freitag, V. Perebeinos, J. Liu, and P. Avouris. Doping and phonon renormalization in carbon nanotubes. *Nature Nanotechnology*, 2(11):725–730, 2007.

[66] T. M. G. Mohiuddin, A. Lombardo, R. R. Nair, A. Bonetti, G. Savini, R. Jalil, N. Bonini, D. M. Basko, C. Galiotis, N. Marzari, K. S. Novoselov, A. K. Geim, and A. C. Ferrari. Uniaxial strain in graphene by raman spectroscopy: G peak splitting, gruneisen parameters, and sample orientation. *Physical Review B*, 79(20):–, 2009.

[67] Y. N. Gartstein, A. A. Zakhidov, and R. H. Baughman. Mechanical and electromechanical coupling in carbon nanotube distortions. *Phys. Rev. B*, 68(11):–, 2003.

[68] L. Pastewka, P. Koskinen, C. Elsasser, and M. Moseler. Understanding the microscopic processes that govern the charge-induced deformation of carbon nanotubes. *Physical Review B*, 80(15):–, 2009.

[69] Cristiano Nisoli, Vincent Crespi, and Eric Mockensturm. The graphenic bicontinuum provides a unified analytical treatment of lattice dynamics in carbon nanostructures. *http://arxiv. org/abs/0704.1305*, 2007.

[70] E. R. Margine, P. E. Lammert, and V. H. Crespi. Reciprocal space constraints create real-space anomalies in doped carbon nanotubes. *Physical Review Letters*, 99(19):–, 2007.

[71] M. Kertesz, F. Vonderviszt, and R. Hoffmann. In *Intercalated Graphites*. Elsevier, m.s. dresselhaus edition, 1983.

[72] L. Pietronero and S. Strässler. Bond-length change as a tool to determine charge transfer and electron-phonon coupling in graphite intercalation compounds. *Phys. Rev. Lett.*, 47(8):593–596, Aug 1981.

[73] C. Y. Li and T. W. Chou. Charge-induced strains in single-walled carbon nanotubes. *Nanotechnology*, 17(18):4624–4628, 2006.

[74] Indhira O. Maciel, Neil Anderson, Marcos A. Pimenta, Achim Hartschuh, Huihong Qian, Mauricio Terrones, Humberto Terrones, Jessica Campos-Delgado, Apparao M. Rao, Lukas Novotny, and Ado Jorio. Electron and phonon renormalization near charged defects in carbon nanotubes. *Nature Materials*, 7(11):878–883, 2008.

[75] I. O. Maciel, J. Campos-Delgado, M. A. Pimenta, M. Terrones, H. Terrones, A. M. Rao, and A. Jorio. Boron, nitrogen and phosphorous substitutionally doped single-wall carbon nanotubes studied by resonance raman spectroscopy. *Physica Status Solidi B*, 246(11-12):2432–2435, 2009.

[76] Anindya Das and A. K. Sood. Renormalization of the phonon spectrum in semiconducting single-walled carbon nanotubes studied by raman spectroscopy. *Physical Review B*, 79(23):235429, 2009.

[77] Peter M. Rafailov, Janina Maultzsch, Christian Thomsen, Urszula Dettlaff-Weglikowska, and Siegmar Roth. Kohn anomaly and electronphonon interaction at the k-derived point of the brillouin zone of metallic nanotubes. *Nano Letters*, 9(9):3343–3348, 2009.

[78] Z. Yao, C. L. Kane, and C. Dekker. High-field electrical transport in single-wall carbon nanotubes. *Physical Review Letters*, 84(13):2941–2944, 2000.

[79] Michele Lazzeri and Francesco Mauri. Coupled dynamics of electrons and phonons in metallic nanotubes: Current saturation from hot-phonon generation. *Physical Review B (Condensed Matter and Materials Physics)*, 73(16):165419–6, 2006.

[80] E. Pop, D. Mann, J. Cao, Q. Wang, K. Goodson, and H. J. Dai. Negative differential conductance and hot phonons in suspended nanotube molecular wires. *Physical Review Letters*, 95(15):155505, 2005.

[81] Nicola Bonini, Michele Lazzeri, Nicola Marzari, and Francesco Mauri. Phonon anharmonicities in graphite and graphene. *Phys. Rev. Lett.*, 99(17):176802, Oct 2007.

[82] S. B. Cronin, Y. Yin, A. Walsh, R. B. Capaz, A. Stolyarov, P. Tangney, M. L. Cohen, S. G. Louie, A. K. Swan, M. S. Unlu, B. B. Goldberg, and M. Tinkham. Temperature dependence of the optical transition energies of carbon nanotubes: The role of electron-phonon coupling and thermal expansion. *Physical Review Letters*, 96(12):–, 2006.

[83] M. Steiner, M. Freitag, V. Perebeinos, J. C. Tsang, J. P. Small, M. Kinoshita, D. N. Yuan, J. Liu, and P. Avouris. Phonon populations and electrical power dissipation in carbon nanotube transistors. *Nature Nanotechnology*, 4(5):320–324, 2009.